GEOLOGY

Paleomagnetic evidence for modern-like plate motion velocities at 3.2 Ga

Alec R. Brenner[1]*, Roger R. Fu[1], David A.D. Evans[2], Aleksey V. Smirnov[3], Raisa Trubko[1,4], Ian R. Rose[2,5]

The mode and rates of tectonic processes and lithospheric growth during the Archean [4.0 to 2.5 billion years (Ga) ago] are subjects of considerable debate. Paleomagnetism may contribute to the discussion by quantifying past plate velocities. We report a paleomagnetic pole for the ~3180 million year (Ma) old Honeyeater Basalt of the East Pilbara Craton, Western Australia, supported by a positive fold test and micromagnetic imaging. Comparison of the 44°±15° Honeyeater Basalt paleolatitude with previously reported paleolatitudes requires that the average latitudinal drift rate of the East Pilbara was ≥2.5 cm/year during the ~170 Ma preceding 3180 Ma ago, a velocity comparable with those of modern plates. This result is the earliest unambiguous evidence yet uncovered for long-range lithospheric motion. Assuming this motion is due primarily to plate motion instead of true polar wander, the result is consistent with uniformitarian or episodic tectonic processes in place by 3.2 Ga ago.

INTRODUCTION

Plate tectonics has been the dominant surface geodynamical regime throughout Earth's recent geological history. One defining feature of modern plate tectonics is the differential horizontal motion of rigid lithospheric plates. The physiography and composition of Earth's modern crust bear evidence for plate tectonic or "mobile-lid" processes including subduction, collisional orogeny, rifting, and ocean spreading. The case for the Archean Earth [4.0 to 2.5 billion years (Ga) ago] is not so clear. The surviving Archean crust consists of ~35 cratons (*1*), most with a characteristic architecture of rounded granitoid intrusive domes rimmed by steeply dipping greenstone keels (*2*). The composition of extant Archean crust is substantially more mafic than modern oceanic crust, with a high fraction of ultramafic rocks such as komatiites (*2*–*4*). These structural and compositional differences have led to a number of proposals that the Archean crust was constructed by exotic processes, including plume tectonics (*5*, *6*), sagduction/drip tectonics (*6*, *7*), and a vertically overturning lithosphere (*8*, *9*). Since some of these processes are difficult to reconcile with plate mobility, alternative geodynamical regimes have been proposed for the Archean Earth, including stagnant-lid and sluggish-lid modes (*10*, *11*) in which the lithosphere was rendered immobile, or at least slowed, due to decoupling from the asthenosphere under elevated geothermal gradients (*12*). Other studies argue for a uniformitarian model of the Archean Earth, in which some variant of modern plate tectonics was in operation at least locally throughout Earth history (*13*). Complete understanding of the Archean lithosphere, hydrosphere, atmosphere, and biosphere are predicated upon distinguishing between these proposed Archean geodynamic modes. Insights into these components of the early Earth are foundational to the inner workings of terrestrial planets generally and what surface conditions and environments hosted the development of the first life.

Arguments for alternative geodynamical regimes in the Archean are often based on inferences of a regime transition toward modern-style plate tectonics. Existing estimates for the age of such a transition range from the Neoproterozoic to the Hadean (see the Supplementary Materials) and invoke a range of observations including global and local geochemical records (*14*–*16*), field relations of possible syn-tectonic rocks (*17*–*19*), and paleomagnetic pole comparisons (*20*–*23*).

A key discriminant between stagnant- and mobile-lid regimes is the rate of horizontal motion of plates over Earth's surface. Absolute plate velocities have typically been ~2 to 10 cm/year (extremes from 0 to 25 cm/year) over the last 400 million years (Ma) (*24*), while hypothesized velocities for stagnant- and sluggish-lid models are typically less than 2 cm/year (*25*). Paleomagnetic methods may constrain the velocity of crustal blocks in deep geological time by measuring their apparent polar wander histories. However, robust paleomagnetic evidence for latitudinal motion has been lacking thus far for times before 2.8 Ga (*20*–*23*). Here, we produce a new paleomagnetic pole from ~3180 Ma volcanics in the East Pilbara Craton of Western Australia and use this result to assess the presence of plate tectonic–like processes on Earth before that time.

Geologic setting of the Honeyeater Basalt

Greenstone belts in the East Pilbara Craton of Western Australia and the Kaapvaal Craton of South Africa are two of the only well-exposed regions on Earth that preserve ≥3.0 Ga rocks metamorphosed to greenschist facies conditions or lower (250° to 500°C, 1 to 8 kbar), making them potentially suitable for paleomagnetic analysis. Archean paleopoles previously reported from the East Pilbara fall into Neoarchean (<2.8 Ga) and Paleoarchean (3.35 to 3.5 Ga) groups (table S3) and are discussed in detail in the Supplementary Materials ("Mesoarchean Paleogeography"). Paleomagnetic study of a rock unit with an intermediate age between existing Paleoarchean and Neoarchean poles can potentially refine the history of East Pilbara motion before 2.8 Ga. One such candidate is the ~3220- to 3170-Ma Soanesville Group (*26*), a predominantly mafic volcano-sedimentary succession that outcrops mainly along the western margin of the East Pilbara. The ~3220- to 3180-Ma lower Soanesville Group is a siliciclastic succession of up to 3500 m of sandstones, turbidites, conglomerates,

[1]Department of Earth and Planetary Sciences, Harvard University, Cambridge, MA, USA. [2]Department of Geology and Geophysics, Yale University, New Haven, CT, USA. [3]Department of Geological and Mining Engineering and Sciences, Michigan Technological University, Houghton, MI, USA. [4]Department of Physics, Harvard University, Cambridge, MA, USA. [5]Department of Earth and Planetary Sciences, University of California Berkeley, Berkeley, CA, USA.
*Corresponding author. Email: alecbrenner@g.harvard.edu

and minor cherts and banded iron formations (*18*). The overlying Honeyeater Basalt (HEB; 3192 to 3176 Ma), which we sampled in this work, contains up to 1050 m of pillowed and massive flows of tholeiitic and komatiitic metabasalt (*18*). The lower Soanesville Group succession is cut by the mafic-ultramafic dikes and sills of the Dalton Suite, which is contemporaneous and probably comagmatic with the HEB (*18*). The 3192 to 3176 Ma age range of the HEB is derived from U-Pb Sensitive High-Resolution Ion Microprobe (SHRIMP) dating of magmatic and detrital zircons and baddeleyites from the Dalton Suite in five greenstone belts (*18*).

Previous studies have hypothesized a rift origin for the Soanesville Group (*18*, *27*, *28*), which may be linked to the initiation of a primitive Wilson cycle (*18*). Its fining-upward siliciclastic succession and subsequent basalts are consistent with a modern rift setting. In addition, the lower siliciclastic portion is syndepositionally deformed by extension and basement-involved normal faulting. If this interpretation is true, the Soanesville Group would represent structural evidence of Mesoarchean horizontal tectonics in the Pilbara Craton.

We sampled from two of the most extensive exposures of the HEB located in the Soanesville Syncline (SVS) and the East Strelley greenstone belt (ESGB; Fig. 1) (*18*). The SVS is a northeast-plunging open syncline that outcrops over an approximately100 km^2 region in the southern Soanesville greenstone belt (*29*). In the ESGB, a baddeleyite-bearing Dalton Suite sill gave a U-Pb SHRIMP age of 3182 ± 2 Ma, in agreement with the 3192 to 3176 Ma age range of the HEB based on U-Pb geochronology throughout the East Pilbara (*18*). Correlation of the HEB across the ESGB and SVS is well established thanks to its unique stratigraphic surroundings. The HEB just overlies a sequence (bottom to top) of komatiites, felsic volcanics, siliciclastics, and banded iron formations (the Kunagunarrina, Kangaroo Caves, Corboy, and Paddy Market Formations, respectively), all intruded by Dalton Suite sills and dikes (*18*). Diagnostically, this sequence repeats itself in both the ESGB and the SVS (*18*). The Corboy Formation is particularly distinctive, as it represents the first thick siliciclastic package in the East Pilbara (*27*). The age of folding in both the SVS and ESGB is ~2930 Ma based on structural comparison with similar folds of this age elsewhere in the Pilbara (*27*). This age corresponds to the widespread emplacement of granitoids of the Sisters Supersuite (c. 2955 to 2920 Ma) across the western Pilbara Craton, including those west of the SVS in the Yule Dome (*27*). Sinistral faulting in the region has been dated to 2936 to 2919 Ma and is synkinematic with granitic intrusions and folding (*29*, *30*).

In both the SVS and ESGB, the HEB is locally weakly metamorphosed to prehnite-pumpellyite facies (*31*), possibly representing the oldest unit in the East Pilbara, or on Earth, not metamorphosed to greenschist facies or higher. In addition, the available range of bedding attitudes across ~2930-Ma structures in both the SVS and ESGB enables a paleomagnetic fold test for constraining the age of magnetization in the HEB.

RESULTS

We extracted and performed thermal demagnetization on 235 oriented cores of the HEB from 22 sites in the SVS and 13 sites in the ESGB (Fig. 1). These samples represent five localities (SVA to SVE; SV indicates Soanesville Syncline) with distinct local bedding attitude from both limbs of the SVS, and two distinct localities (ESA and ESB; ES indicates East Strelley) in the ESGB. Together, these samples potentially permit two separate fold tests in the SVS and ESGB.

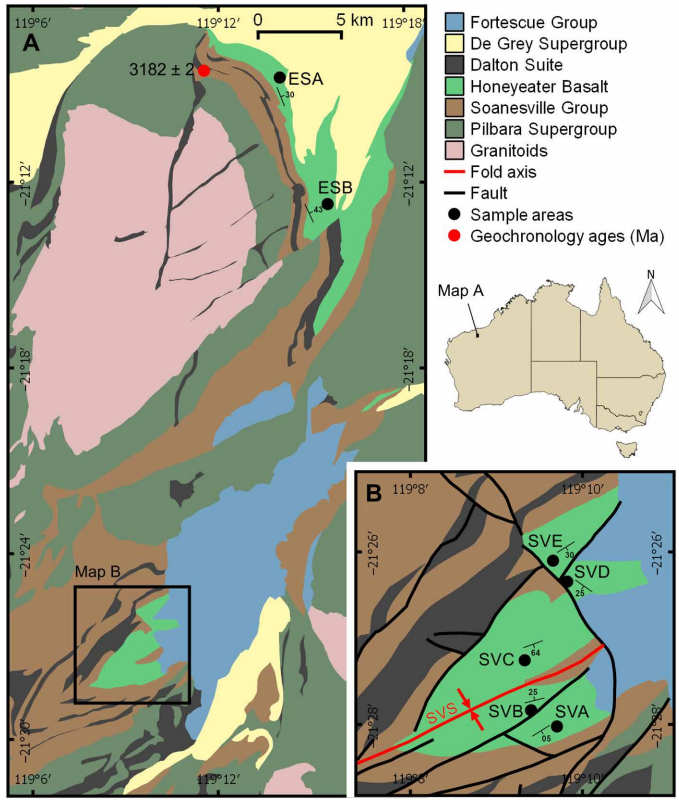

Fig. 1. Map of sampling localities. The HEB (light green) is especially well preserved in the Soanesville Syncline [SVS; see inset Map (**B**)] and East Strelley greenstone belt [ESGB; top of Map (**A**)], along with the underlying Soanesville Group sediments (brown) and Dalton Suite mafic intrusives (dark gray). The age of the HEB (3192 to 3176 Ma) in this area is derived from the age of the coeval Dalton Suite intrusives [e.g., one sample dated to 3182 ± 2 Ma in the ESGB (*18*)].

We identified three overprinting components of magnetization common to most samples. One component ("AF," alternating field) is unblocked by liquid nitrogen treatment and AF demagnetization up to 9 to 10 mT in 225 samples (Fig. 2). This component shows random directions in both in situ and stratigraphic coordinates with no observed relationship to the directions recovered during thermal demagnetization. Upon thermal demagnetization, a low-temperature component (L) found in 198 samples unblocks between ~75° and 300°C (Figs. 2 and 3A and fig. S2). Its direction in in situ coordinates (D, I = 357.4°, −44.2°; α_{95} = 7.0°) is consistent with the present-day geomagnetic field direction (I = −38.2° assuming a current Geocentric Axial Dipolar (GAD) geometry). We therefore conclude that the L component of magnetization is a recent viscous remanent magnetization. A medium-temperature component (M) appears in 181 samples, unblocks within ~200° to 500°C, and consistently displays a shallow northwest-upward mean direction in in situ coordinates (D, I = 310.3°, −19.0°; α_{95} = 5.7°) (Figs. 2 and 3A and fig. S2). In many samples from the SVS, a substantial fraction of this component unblocks between 315° and 355°C, suggesting the presence of pyrrhotite. We interpret the M component as a partial thermoremanent magnetization (pTRM) overprint acquired during low-grade regional metamorphism, possibly during the 2215- to 2145-Ma Ophthalmian Orogeny (*32*) or the 1830- to 1780-Ma Capricorn Orogeny, associated with tectonic accretion along the southern Pilbara margin or subsequent regional tectonic reactivation (*33*). This overprint direction is

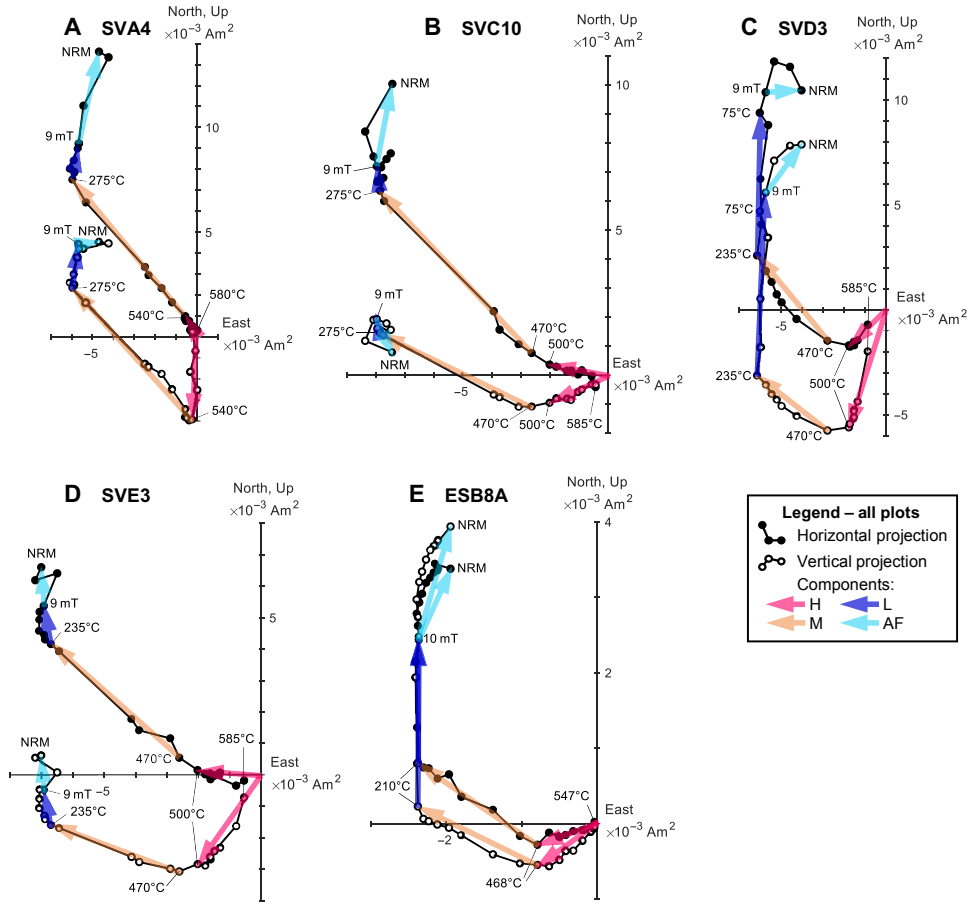

Fig. 2. Orthogonal projection diagrams of representative samples. All are in in situ coordinates and show four components; AF, light blue; L, dark blue; M, orange; and H, magenta (see the main text for discussion). (**A**) Sample SVA4. (**B**) SVC10. (**C**) SVD3. (**D**) SVE3. (**E**) ESB8A.

similar to the reversed counterparts of overprint directions from the Hamersley Basin and Tom Price iron formations (D, I ~ 305°, −10°) (*34*). Our interpretation of this magnetization as a metamorphic pTRM is also consistent with its typical maximum unblocking temperature range of ~400° to 500°C. The corresponding metamorphic temperature range in single-domain magnetite-dominated samples assuming time scales of 10 to 100 Ma for orogenesis is ~250° to 400°C (*35*), overlapping the conditions of prehnite-pumpellyite facies metamorphism observed in the HEB within our study area (*31*) (fig. S3).

The highest-temperature component of magnetization ("H") unblocks between ~400° and 590°C in 128 samples (Fig. 2). This maximum unblocking temperature and its origin-trending direction suggest that the H component is a magnetite-hosted TRM or thermochemical remanent magnetization (TCRM). In localities SVB and ESA, no sites showed coherence in H component directions and were thus excluded from further analysis. Localities SVA, SVC, SVD, SVE, and ESB contained between two and three sites each with coherent within-site directions ($n \geq 2$, $k \geq 15$; table S1). Site mean directions in these localities display reasonable scatter around the locality mean, with k values between 10 and 66, while locality means are mutually scattered in in situ coordinates (Fig. 3A).

After correction for folding (see Materials and Methods), localities SVA, SVC, SVD, and SVE H component site and locality means cluster about a southwest and down direction (D, I = 203.7°, 59.0°; α_{95} = 11.3°; N = 12 sites; Fig. 3B and table S1). A three-limb fold test (*36*) using directions from SVC, SVD, and SVE using the nominal mapped SVS geometry (trend/plunge = 069°/41°) (*29*) passes with minimum scatter at 100 ± 30% (2σ) unfolding (Fig. 3C). Inclusion of locality SVA shifts the point of minimum scatter to ~79 ± 22% unfolding (Fig. 3D). In general, such an intermediate degree of unfolding at peak concentration may be due to subtle amounts of component mixing, diachronous magnetizations, syn-folding magnetization acquisition, local structural variability within the fold, or unrecognized vertical axis rotation (*36*). A final possibility is that the high-temperature magnetization in SVA cooling units was acquired over a short time interval insufficient for averaging paleosecular variation.

The steep H direction of SVA is similar to that of the ~2750-Ma Mount Jope Volcanics (MJV) (*37*). This possibility is unlikely, however, since the MJV pole was reported only from lavas in the Hamersley ranges far to the south, and the SVS-ESGB region is much closer to other Fortescue Group lavas (e.g., P0) with substantially different directions (*37*). The low metamorphic grade of the HEB and its ferromagnetic mineralogy (see below) also provide evidence against complete ~2930-Ma, syn-folding remagnetization. Further, although SVA is situated on a small fault-bounded block that may have rotated relative to the north limb of the syncline, the steep inclination of the SVA locality H directions implies that vertical axis rotations cannot substantially improve the concentration of unfolded directions. On the other hand, the high among-site precision parameter of SVA

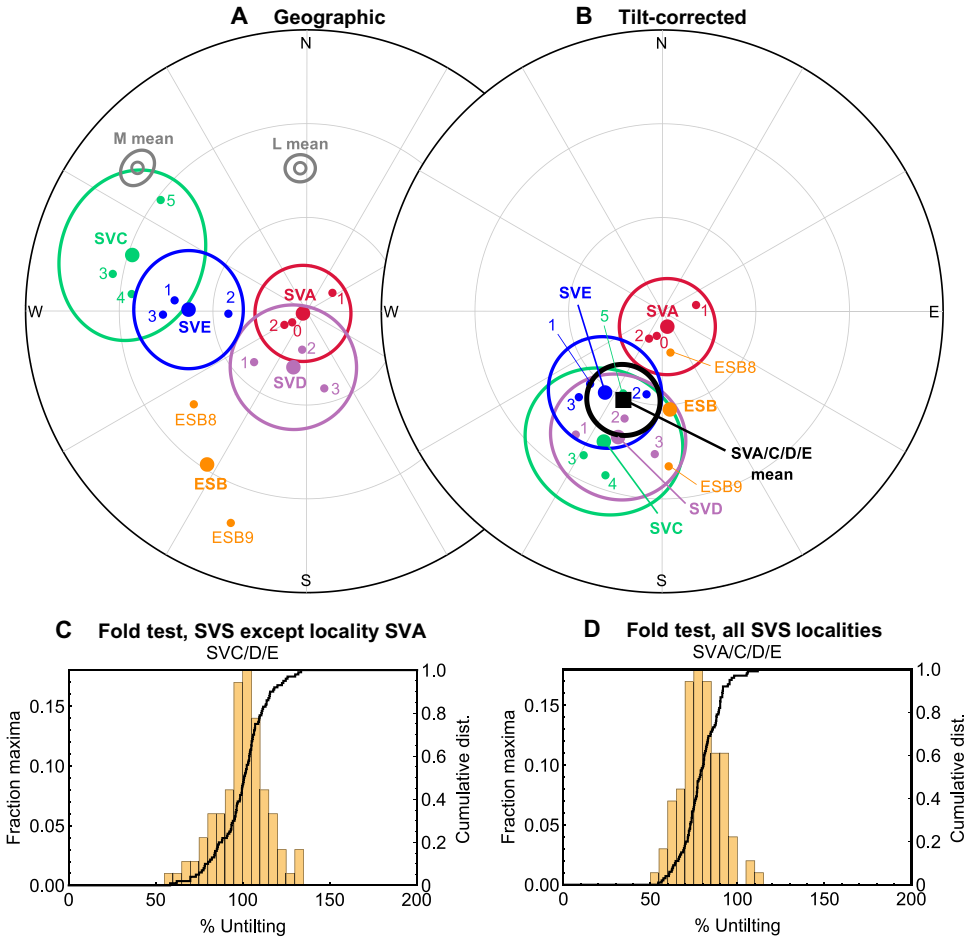

Fig. 3. Fold test on the H component. Equal-angle stereonet projections show measured directions in (**A**) in situ and (**B**) 100%-fold–corrected coordinates. Mean H component directions from each site (small points) are color-coded by locality means (large points with error circles; SVA, red; SVC, light green; SVD, light purple; SVE, blue; ESB, orange). The large error circle is omitted from the ESB mean direction for clarity. L and M component in situ means are gray. The tilt-corrected mean of all sites in SVA, SVC, SVD, and SVE is shown in black. Tilt correction in (B) includes correction for the plunge of the SVS fold axis. (**C**) Histogram (orange bars) and cumulative distribution (bold curve) of maximum post-unfolding fit in a fold test on the SVC, SVD, and SVE directions after Tauxe and Watson (*36*), using the 069°/41° mapped axis of the SVS. The fold test passes with best-fit unfolding 100 ± 15%. (**D**) A fold test on the SVA, SVC, SVD, and SVE directions with best fit at 79 ± 11% unfolding.

(k = 65.4), which is the highest of our sampled localities, supports the hypothesis that the site directions are not adequately sampling paleosecular variation. Such a scenario would apply, for instance, to a set of flows erupted in rapid succession atop one another, such as on the south flank of Kilauea, Hawai'i today, such that paleosecular variation is minimal over the time intervals between sites. We therefore posit that the SVA directions are biased by insufficient sampling of paleosecular variation, although an age of emplacement near 3180 Ma but distinct from SVC, SVD, and SVE by at least several million years cannot be ruled out. The latter scenario would imply substantial latitudinal velocity by ~3.18 Ga. In either case, positive fold test in three SVS localities constrains the age of the H component to at least 2930 Ma (*27*).

Area ESB's distinct direction may be attributable to its location within the ESGB block, which may have undergone unknown structural rotation with respect to the SVS (see the "Tests for Archean plate motion" section). While the placement of ESB supports its exclusion from our analysis, the similarity of the ESB H component direction (D, I = 175.5°, 58.5°; α_{95} = 89.1°; N = 2 sites; Fig. 3B and table S1) to those in the SVS hints at consistency of this component across multiple fold structures. Further sampling of HEB lavas with a range of bedding attitudes in the ESGB would be required to produce a fold test that could include locality ESB. We limit further discussion to our preferred H component direction and pole defined by localities SVA, SVC, SVD, and SVE.

Petrological and rock magnetic properties of the HEB may provide further insight into the timing of remanence acquisition. The low metamorphic grade of the HEB relative to the 590°C maximum unblocking temperature of the H component rules out a thermal overprint origin after 3182 Ma. To constrain the origin of H magnetization, we mapped the spatial distribution of magnetic sources hosting the natural remanent magnetization (NRM) using a Quantum Diamond Microscope (QDM; see Materials and Methods) (*38*). For this analysis, we chose SVD14, a sample with a very strong H component relative to total NRM moment (J/J_0 = 61%). The strongest sources of NRM were visible under an optical microscope as dark, opaque, sub-equant grains <5 μm in size, which is consistent with rock magnetic experiments on two samples from site ESB8 identifying pseudo-single-domain (PSD) magnetite as the major remanence-hosting phase (fig. S5). We find that these H magnetization-carrying

grains are localized along the rims of several-millimeter laths of skeletal augite surrounding chlorite cores, most likely originally zoned clinopyroxenes where the cores were serpentinized to chlorite on the seafloor (figs. S3 and S4). The textural association of magnetic sources with the rims of these relict zoned pyroxene grains, in conjunction with rock magnetic data, suggests that they consist of magnetite precipitated during serpentinization, during which the reaction front would have been localized to the contact between the altering phases and the surrounding high-temperature fluids (*39*). The H component therefore likely represents a shortly post-emplacement seafloor TCRM, implying that the H magnetization was acquired near the time of eruption.

We measured magnetic hysteresis loops, backfield remagnetization of saturation remanence, and temperature dependence of low-field magnetic susceptibility (see Materials and Methods) on two samples with well-defined H components from site ESB8. The magnetic hysteresis behavior in both samples is dominated by paramagnetism (likely from clays). After paramagnetic slope correction, the measured magnetic hysteresis loops have a regular shape and indicate the presence of a low-to-intermediate coercivity magnetic phase (H_c = 6 to 11 mT; fig. S5, A and B). Magnetic hysteresis data did not reveal the presence of magnetically hard phases such as hematite. The M_{rs}/M_s (saturation remanence to saturation magnetization) and H_{cr}/H_c (coercivity of remanence to coercive force) ratios (ESB8B: M_{rs}/M_s = 0.076 and H_{cr}/H_c = 3.72; ESB8G: M_{rs}/M_s = 1.42 and H_{cr}/H_c = 3.00) suggest PSD magnetite (*40*, *41*) as a remanence carrier in both samples (fig. S5C).

The low-field susceptibility [$k(T)$] curves measured from ESB8B and ESB8G are irreversible, suggesting heating-induced alteration (fig. S5, D and E). For both samples, the preheating low-temperature $k(T)$ run shows a monotonic decrease of k with increasing temperature, whereas the high-temperature heating legs indicate the presence of a magnetic mineral phase with a broad (~400° to 600°C) range of Curie temperatures (T_c). We interpret this phase as cation-deficient magnetite. The strongly irreversible behavior observed above 600°C may indicate an additional metastable iron-rich phase with T_c > 700°C formed by thermal alteration of paramagnetic minerals (e.g., clays) (*42*). This phase subsequently converts to nearly stoichiometric magnetite as indicated by the Hopkinson peak at ~580° to 600°C seen in the cooling $k(T)$ legs for both samples and by the well-expressed Verwey transition (*43*) in the post-heating low-temperature $k(T)$ curves. The irreversible signal above 600°C may also be partially due to paramagnetic minerals directly converting to a nearly magnetite phase. The broader humps on the cooling legs of high-temperature $k(T)$ runs likely represent primary titanomagnetite (with the Curie temperatures shifted to lower values, potentially, due to stress relaxation during thermal treatment). In summary, these rock magnetic measurements are fully consistent with the magnetic mineralogy identified from our micromagnetic imaging experiments.

On the basis of the fold test result, the uniquely low metamorphic temperature of the HEB, the petrographic context of the remanence-carrying grains, and the high unblocking temperature and origin-trending nature of H magnetization, we conclude that the H component is a primary TRM or TCRM dating to emplacement of the HEB at 3182^{+10}_{-6} Ma ago (*18*). The paleopole for this direction (λ, ϕ = 60.6°S, 83.9°E; α_{95} = 15.3°), which we call the HEBh pole for "HEB, high temperature," corresponds to a paleolatitude of λ_p = 43.7° ± 15.3° (Figs. 4and 5A and table S2). The HEBh pole reduces the size of the largest unsampled gap in the available (i.e., after 3.5 Ga) paleomagnetic record (the ~580 Ma separating poles EBm and P0) by 170 Ma.

Accepting a primary origin for the H magnetization, the angular dispersion of its virtual geomagnetic poles (VGPs) may be used to characterize the variability of the geodynamo during the Mesoarchean. We compute an angular standard deviation of S_B = 19.5° ± 7.9° (N = 11 VGPs). This is greater than the ~12° dispersion expected at ~45° paleolatitude based on a fit to 2.2- to 3.0-Ga poles (*44*) and somewhat greater than values of S_B observed over the last 5 Ma (*45*). VGPs of the older, lower-latitude Duffer Formation (DFM) pole (*46*) show lower scatter with S_B = 9.7° ± 5.5° (N = 11 VGPs), potentially suggesting a more stable pre–3.0-Ga geodynamo. An important caveat of these calculations is that both have small sample sizes, which may bias S_B to lower values (*47*). In addition, the probable early serpentinization origin of the H magnetization complicates the interpretation of its VGP dispersion, as magnetite ingrowth may have occurred over periods long enough to partially average paleosecular variation. Chemical remanence directions are also commonly more scattered than thermal remanence directions [e.g., in serpentinized ultramafic intrusions (*48*)]. However, many sites display coherent directions distinct from those of adjacent sites, demonstrating that some directional changes due to paleosecular variation were indeed recorded and supporting our interpretation that the observed inter-site scatter reflects geodynamo stability.

DISCUSSION

Tests for Archean plate motion

Together with paleolatitudes from other poles previously reported from the East Pilbara, the new HEBh pole places new lower bounds on the horizontal drift rate of the East Pilbara between ~3.35 and 2.77 Ga relative to Earth's rotation axis, assuming a geocentric axial dipole field geometry at ~3.2 Ga. The youngest pre-HEBh pole from the East Pilbara is that of the 3350- to 3335-Ma Euro Basalt (EBm), which provides an estimated paleolatitude of 8.09° ± 5.3° (*49*). This paleolatitude is distinguishable from that of the HEB at 2σ and requires that the average latitudinal velocity of the Pilbara exceeded 0.23° ± 0.10°/Ma or ≥2.50 ± 1.15 cm/year between 3.35 and 3.18 Ga (Fig. 5). The oldest post-HEBh pole is that of Fortescue Group Package 0 (P0), with an age most likely within 10 Ma of its minimum age of 2772 ± 2 Ma (*37*, *50*). Its paleolatitude of 57.3° ± 8.0° implies an average latitudinal velocity of 0.03° ± 0.04°/Ma for the Pilbara between 3.18 and 2.77 Ga or ≥0.37 ± 0.47 cm/year (Fig. 5). These values are lower bounds on the rate of lithospheric motion for several reasons. The longitude of the Pilbara during the relevant time interval is unknown, implying that all above drift rates are lower bounds. In addition, the unknown polarity of the geomagnetic field precludes these rates from accounting for the sign of the paleolatitude.

In addition to the latitudinal translations quantified by inclination changes, declination changes between the P0, HEBh, and EBm poles may imply substantial vertical axis rotations. Approximately 124° of clockwise (CW) rotation occurred in the ~170 Ma between the EBm and HEBh poles (0.73°CW/Ma) and ~101° of counterclockwise (CCW) rotation in the ~410 Ma between the HEBh and P0 poles (0.25°CCW/Ma). These rotations may originate from plate-tectonic motion of the East Pilbara Craton, true polar wander (TPW), or post-emplacement local block rotations, perhaps during ~2950- to 2930-Ma deformation in the Lalla Rookh-Western Shaw Structural Corridor (LWSC) that sinistrally sheared the majority of the SVS and

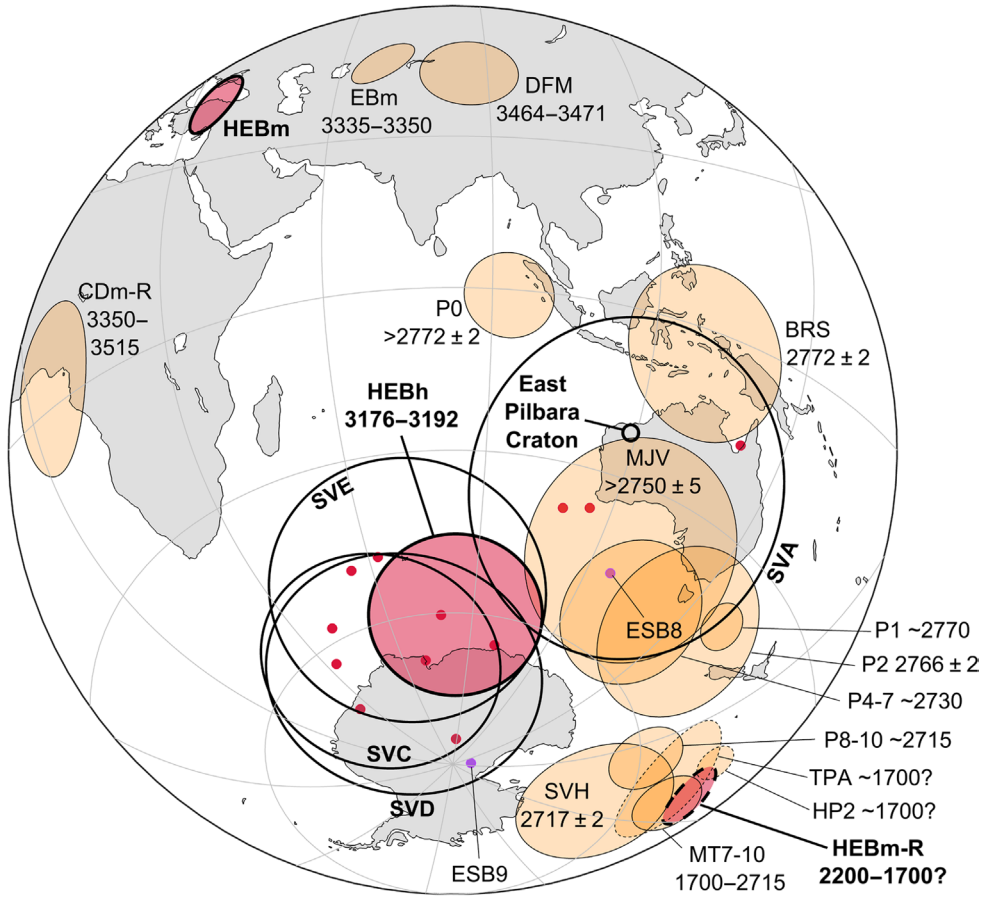

Fig. 4. Paleopoles from the Pilbara Craton. Stratigraphic coordinates apply except for HEBm and HEBm-R overprints in in situ coordinates. Numbers are ages in million years. Poles on the hemisphere opposite the viewer have dashed outlines. Poles reported in this study are red-filled circles and ellipses, locality-mean poles are black hollow circles, and site VGPs are red points (ESB sites in purple; ESB locality-mean pole not shown for clarity). Poles from other studies in the Pilbara are orange.

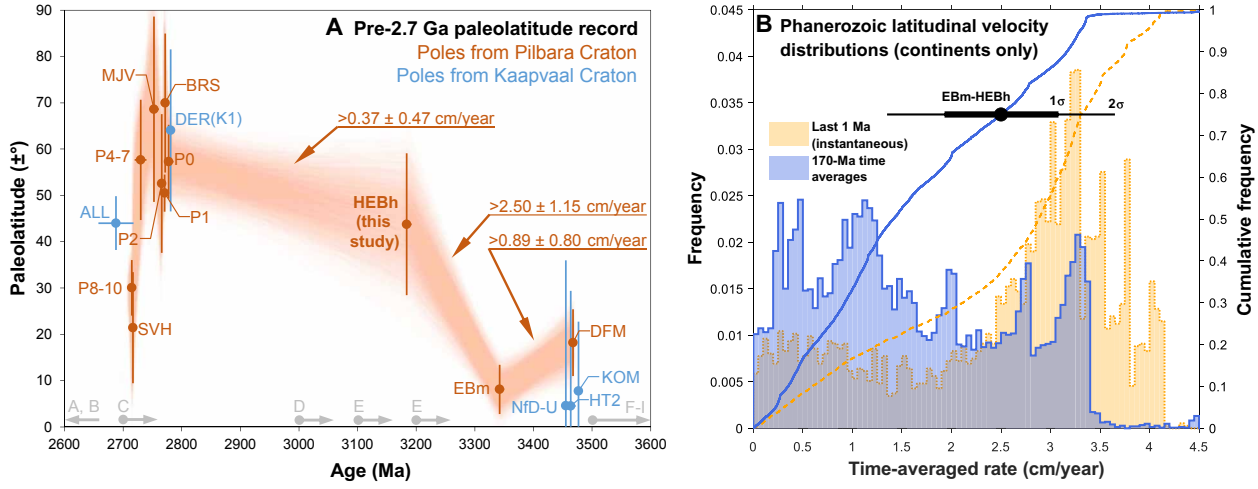

Fig. 5. Tests for Archean plate motion. (**A**) Meso-Paleoarchean paleolatitude records from the Pilbara Craton (Western Australia, orange) and Kaapvaal Craton (South Africa, blue), including this study (HEBh). Paleolatitude error bars are 2σ; age error bars are 2σ or the full range allowable given available constraints. The orange shaded region is a sample of the range of minimum-velocity paths allowed by existing poles. Gray arrows at the bottom are constraints on the onset date of mobile-lid plate tectonics from a sample of previous studies, with letters referencing studies listed in the Supplementary Materials. (**B**) Distributions of time-averaged latitudinal velocities on the continents (*24*) recorded at $N = 3736$ randomly selected points from the present to 1 Ma (yellow with dashed lines) and over 170 Ma windows throughout the Phanerozoic (blue with solid lines) as both histograms and cumulative distribution frequencies (line overlays). The 170 Ma distribution tends toward slower rates because it often samples reversals in plate velocity. For comparison, the minimum motion rate implied by the EBm and HEBh poles is shown by the black point and error bars. This rate, which is averaged over a 170 Ma interval, is comparable with geologically modern rates.

ESGB (*29*, *30*). The region in which the EBm pole was measured (*49*) would not have rotated substantially during this episode (*29*, *30*). Local effects related to the impingement of the nearby Shaw, Yule, and Strelley batholiths apparently both produced the SVS and rotated its central portion CW (*29*, *30*), thus potentially accounting for some of the observed EBm-HEBh rotation. This would also imply that the rotation measured between the HEBh and P0 poles is an underestimation, since CW structural rotation in the LWSC would reduce the observed CCW rotation. Regardless, we cannot determine whether either of the observed vertical axis rotations is due to purely local structural effects, rotation of the entire East Pilbara, or a combination of both processes.

The paleomagnetic record thus indicates that the East Pilbara experienced horizontal motion of ≥2.50 ± 1.15 cm/year in the ~170 Ma between 3350 and 3180 Ma and ≥0.37 ± 0.47 cm/year in the ~410 Ma between 3180 and 2772 Ma (Fig. 5A). The former rate is generally inconsistent with hypothesized "hard" stagnant-lid surface velocities and observed rates of Phanerozoic net lithosphere rotation (typically <2 cm/year) (*25*, *51*). It falls between the 48th and 99th percentiles of the Phanerozoic distribution (since 410 Ma) of latitudinal continental plate velocities (*24*) time-averaged over 170 Ma windows, as estimated from random point sampling of continental lithosphere (Fig. 5B; see Materials and Methods). We chose these windows to cover the last full Wilson cycle, sampling from the full range of tectonic settings encountered on the geodynamically "modern" Earth (figs. S6 and S7). The paleolatitudinal velocity of the Pilbara between 3.35 and 3.18 Ga is therefore comparable to those observed in modern plate motion, conforming to either a uniformitarian or episodic model of Archean tectonics (Fig. 5B). An episodic regime would combine a stagnant-lid state with occasional rapid mobile-lid plate motion (*52*) and is possible for both the pre– and post–3.18-Ga periods. In this case, our minimum rates would represent a mix of substantial tectonic drift velocities (>2.50 cm/year) and episodes of slower motion. Hence, we cannot rigorously rule out episodic transitions between a stagnant- or sluggish-lid regime and intervals of modern-style tectonics before 2.8 Ga without further paleomagnetic studies sampling the motion of multiple Archean cratons over identical, closely spaced time intervals.

The relative contributions of TPW (*53*, *54*) and differential plate motion to these rates are unknown, representing another opportunity for further work. Resolving the TPW and differential components of motion during 3.35 to 3.18 Ga would require ~3.35-Ga and 3.18-Ga paleopoles from another craton. Distinguishing between these contributions to net motion is an important test of Archean tectonic style, since motion of a stagnant lid would manifest as a net rotation of the lithosphere (i.e., indistinguishable from TPW in the paleomagnetic record), while mobile-lid tectonic processes would produce substantial differential motion. Measurement of substantial TPW during the Archean would be a noteworthy result, suggesting a less stable moment tensor, and perhaps more vigorous convection or a hemispherically asymmetric lithosphere.

CONCLUSIONS

While plate tectonics have characterized Earth's geodynamics in recent geologic time, it is unknown whether long-range horizontal motion of lithospheric plates occurred before ~2.7 Ga. Resolving this uncertainty would fundamentally contribute to understanding the formation settings of Earth's earliest crust and nascent biosphere and the evolution of geodynamics in terrestrial planets in general. We use paleomagnetic methods to isolate a high-temperature magnetization in the 3180-Ma HEB of the East Pilbara Craton that unblocks beyond the peak metamorphic temperature of the basalt (~250°C). The restored paleomagnetic directions robustly pass a fold test within the ~2930-Ma SVS. These observations, combined with magnetic microscopy and rock magnetic results, suggest a primary origin for the magnetization. This result establishes a paleolatitude of 43.7° ± 15.3° for the East Pilbara at ~3180 Ma and substantially reduces the duration of the longest unsampled gap in the available paleomagnetic record. With this new record, we show that paleolatitudes of the East Pilbara require an average latitudinal drift rate of at least 0.23°/Ma or 2.50 cm/year between 3350 and 3180 Ma. Since this time-averaged rate of horizontal motion is typical of modern plates, the paleomagnetic record is suggestive of either uniformitarian or episodic operation of plate tectonics in the East Pilbara before ~3.2 Ga. We cannot yet distinguish between differential plate motion, TPW, and net rotation explanations for the observed latitudinal motion, nor can we rule out modern-style or episodic plate tectonic motion before 3180 Ma. Constraining the relative contributions of each of these components represents a promising direction for future paleomagnetic studies in the East Pilbara and other cratons.

MATERIALS AND METHODS

We extracted 235 oriented cores of the HEB from 22 sites in the SVS (Fig. 1B) and 13 sites in the ESGB (Fig. 1A). These samples represent five localities (SVA to SVE) with distinct local bedding attitude from both limbs of the SVS and two distinct localities (ESA and ESB) in the ESGB. We drilled and field-oriented five to nine 2.5-cm core samples per site using magnetic and solar compasses while avoiding topographically prominent outcrops susceptible to lightning strikes where possible. Within each locality, we used a single paleohorizontal (bedding) attitude across all sites, thus attempting to average local variability of bedding attitudes we measured on rubbly flowtops and potentially undulatory chert interbeds.

We measured the magnetic moment of core samples using 2G Enterprises Model 755 Superconducting Rock Magnetometers at the Massachusetts Institute of Technology Paleomagnetism Laboratory and the Yale Paleomagnetic Facility. We subjected the SVS samples to AF demagnetization up to 9 mT in steps of 3 mT followed by thermal demagnetization up to 590°C in steps of 10° to 40°C. For ESGB samples, we first subjected them to immersion in liquid nitrogen to minimize the signal of multi-domain magnetite grains. We then applied AF demagnetization up to 10 mT in steps of 1 mT followed by thermal demagnetization up to 590°C in steps of 10° to 60°C. For some samples in the SVS, we averaged pairs of the highest-temperature demagnetization steps (>500°C) to suppress noise and to correct for a weak laboratory thermal remanence acquired in the oven. Because the cores were oriented such that they alternately pointed into and out of the oven during thermal demagnetization steps, this weak remanence, which was oriented approximately along the oven axis, was effectively eliminated by averaging pairs of thermal steps.

We quantified the directions of magnetization components using principal components analysis (*55*) and excluded components with mean angle of deviation greater than 20° from further analysis. For all but seven samples in which the highest-temperature component was not origin trending (likely as a result of weak pTRMs

acquired within the oven), we forced the highest-temperature component of magnetization to include the origin. Use of non–origin-forced fits to all samples did not significantly change our results. We also rejected data from 20 samples that displayed strong, single-component origin-trending magnetizations characteristic of lightning remagnetization. We then calculated site mean directions from sample components after removal of 30 samples with outlier directions. Outliers were samples with H component directions that differed from well-clustered H components from other samples within the same site by more than ~30°, often because H component fits in such samples were based on too few points to reliably average noise in the demagnetization path. We retained in our analysis sites with at least two passing core samples and within-site Fisher precision parameter $k \geq 15$.

To compute the correct paleomagnetic directions in bedding coordinates, we determined the trend and plunge of the SVS fold hinge to be 069°/41° based on mapped bedding orientations (*29*). We therefore rotated site mean directions by 41° around the horizontal axis with trend 159° and applied a second horizontal axis rotation based on field observations of lava flow bedding attitudes to restore local paleohorizontal. Samples from the ESGB required only a single horizontal axis rotation to restore their original orientation, as the plunge of the SVS does not apply to the rocks of the ESGB.

To identify the remanence-carrying magnetic grains, we observed oriented sections of several cores with the QDM (*56*) at the Harvard Paleomagnetics Laboratory. The QDM uses optically detected magnetic resonance spectroscopy of nitrogen-vacancy (NV) centers in a diamond to produce maps of the surface vector magnetization on the samples with several-millimeter field of view and ~2-μm resolution. From each sample, we prepared a 1- to 2-mm-thick, 25-mm-diameter disk-shaped section and polished its upper face using 1-μm Al_2O_3 grit, taking care to avoid overprinting the sample's NRM. Placing the polished face of our samples in contact with the sensing diamond, we measured the magnetic field intensity along the [111] direction of the diamond crystal lattice using projective magnetic microscopy (*56*). We isolated the magnetic field signal of the ferromagnetic grains by measuring the sample successively under two mutually antiparallel 0.9 mT bias fields and computed the out-of-plane (B_z) magnetic field using a spectral algorithm (*57*). Once we located magnetic sources in these maps, we used a Horiba Scientific XploRA Plus Raman microscope (532 nm excitation wavelength) to identify the mineral phases surrounding them, thus providing petrographic context for the source(s) of remanence.

We measured magnetic hysteresis parameters (coercivity, H_c; coercivity of remanence, H_{cr}; saturation remanence, M_{rs}; and saturation magnetization, M_s) at room temperature using a Model 2900 Princeton Measurement Corporation Alternating Gradient Field Magnetometer at Michigan Tech. We used a maximum applied field of 1 T for magnetic hysteresis loops and of 0.5 T for backfield demagnetization of M_{rs} measurements. We also measured temperature dependences of low-field magnetic susceptibility [$k(T)$] upon cycling the samples between room temperature and 700°C (in argon) using an AGICO MFK1-FA magnetic susceptibility meter equipped with a high-temperature furnace and cryostat at Michigan Tech. The $k(T)$ curves were also measured upon heating from ~−180°C to room temperature before and after the high-temperature thermomagnetic runs. The field applied in all $k(T)$ experiments was 250 μT.

To measure paleosecular variation captured by the HEBh pole, we calculated the angular standard deviation S_B of its VGPs using the within-site dispersion correction after Doell (*58*)

$$S_B = \sqrt{S_{tot}^2 - \frac{S_w^2}{\bar{n}}} = \sqrt{\frac{1}{N-1}\sum_{i=1}^{N}\Delta_i^2 - \frac{1}{N}\frac{\left(\sum_{i=1}^{N}\frac{81^\circ}{\sqrt{K_{wi}}}\right)^2}{\sum_{i=1}^{N} n_i}} \quad (1)$$

where N is the number of sites each with n_i samples, S_{tot} is the total dispersion, S_w is the average within-site dispersion, $\bar{n}$ is the average number of samples per site, Δ_i is the angular distance between the ith VGP and the mean of all N VGPs, and K_{wi} is the precision parameter of sample VGPs within the ith site. We calculated K_{wi} from individual site direction precisions k_i and paleolatitudes λ_i after Cox (*59*)

$$K_{wi} = k_i\left[\frac{1}{8}(5 + 18\sin^2\lambda_i + 9\sin^4\lambda_i)\right]^{-1} \quad (2)$$

We used only VGPs from localities SVA, SVC, SVD, and SVE and adopted a common cutoff angle of $\Delta_i < 45°$ to exclude transitional directions (*44*, *60*). We then used jackknife ($N-1$) resampled values S_{Bi} of the mean $\bar{S}_B$ and estimated its uncertainty σ_{SB} after Efron (*61*)

$$\sigma_{S_B} = \sqrt{\frac{N-1}{N}\sum_{i=1}^{N}(S_{Bi} - \bar{S}_B)^2} \quad (3)$$

We used Monte Carlo resampling ($N = 10^6$) of the ages and paleolatitudes of each pole pair to estimate the uncertainty range of latitudinal plate motion rates between them. For poles DFM, EBm, HEBh, and P0, we assumed normally distributed age uncertainties with mean ± 2σ values 3467.5 ± 3.5, 3342.5 ± 7.5, 3184 ± 8, and 2778 ± 8 Ma, respectively. We took each pole's paleolatitude uncertainty to be normally distributed about its mean with $2\sigma = \alpha_{95}$. We converted rates from degrees per million years to centimeters per year with the factor 11.1 (cm/year)/(°/Ma).

To evaluate whether the latitudinal motion rates we measure are consistent with a mobile-lid setting, we selected 10,000 randomly distributed latitude and longitude points and filtered these to those on the continents only ($N = 3736$) since the HEB erupted atop the western margin of East Pilbara continental crust. We displaced these points from their present to their reconstructed positions at 1 Ma (i.e., over the 0- to 1-Ma window) and bracketing four 170-Ma-long windows (0 to 170, 80 to 250, 160 to 330, and 240 to 410 Ma) throughout the last Wilson cycle (fig. S6). We reconstructed points using GPlates with the paleomagnetic reference frame and the 410-Ma to present plate motion model of Matthews *et al.* (*24*). We then calculated the latitudinal displacement of all points across each reconstructed window. The distribution of latitudinal changes over the last 1 Ma approximates the instantaneous latitudinal drift rate distribution. The distribution over the total of all four 170 Ma windows simulates the distribution of rates calculated from two samples from the same location but 170 Ma apart, as is the case for the EBm and HEBh poles.

SUPPLEMENTARY MATERIALS

Supplementary material for this article is available at http://advances.sciencemag.org/cgi/content/full/6/17/eaaz8670/DC1

REFERENCES AND NOTES

1. W. Bleeker, The late Archean record: A puzzle in ca. 35 pieces. *Lithos* **71**, 99–134 (2003).
2. P. Thurston, Greenstone belts and granite–greenstone terranes: Constraints on the nature of the archean world. *Geosci. Can.* **42**, 10.12789/geocanj.2015.42.081 (2015).

3. M. Tang, K. Chen, R. L. Rudnick, Archean upper crust transition from mafic to felsic marks the onset of plate tectonics. *Science* **351**, 372–375 (2016).
4. N. D. Greber, N. Dauphas, A. Bekker, M. P. Ptáček, I. N. Bindeman, A. Hofmann, Titanium isotopic evidence for felsic crust and plate tectonics 3.5 billion years ago. *Science* **357**, 1271–1274 (2017).
5. M. J. Van Kranendonk, Two types of archean continental crust: Plume and plate tectonics on early earth. *Am. J. Sci.* **310**, 1187–1209 (2010).
6. R. Fischer, T. Gerya, Early earth plume-lid tectonics: A high-resolution 3D numerical modelling approach. *J. Geodyn.* **100**, 198–214 (2016).
7. E. Sizova, T. Gerya, K. Stüwe, M. Brown, Generation of felsic crust in the Archean: A geodynamic modeling perspective. *Precambrian Res.* **271**, 198–224 (2015).
8. D. Chardon, P. Choukroune, M. Jayananda, Strain patterns, décollement and incipient sagducted greenstone terrains in the Archaean Dharwar craton (south India). *J. Struct. Geol.* **18**, 991–1004 (1996).
9. D. Wiemer, C. E. Schrank, D. T. Murphy, L. Wenham, C. M. Allen, Earth's oldest stable crust in the Pilbara Craton formed by cyclic gravitational overturns. *Nat. Geosci.* **11**, 357–361 (2018).
10. A. Lenardic, The diversity of tectonic modes and thoughts about transitions between them. *Philos. Trans. A Math. Phys. Eng. Sci.* **376**, 20170416 (2018).
11. J. H. Bédard, Stagnant lids and mantle overturns: Implications for Archaean tectonics, magmagenesis, crustal growth, mantle evolution, and the start of plate tectonics. *Geosci. Front.* **9**, 19–49 (2018).
12. J. Korenaga, Archean geodynamics and the thermal evolution of Earth. *Geophys. Monogr. Am. Geophys. Union* **164**, 7–32 (2006).
13. B. Keller, B. Schoene, Plate tectonics and continental basaltic geochemistry throughout Earth history. *Earth Planet. Sci. Lett.* **481**, 290–304 (2018).
14. B. Dhuime, C. J. Hawkesworth, P. A. Cawood, C. D. Storey, A change in the geodynamics of continental growth 3 billion years ago. *Science* **335**, 1334–1336 (2012).
15. J. Korenaga, Crustal evolution and mantle dynamics through Earth history. *Philos. Trans. A Math. Phys. Eng. Sci.* **376**, 20170408 (2018).
16. S. B. Shirey, S. H. Richardson, Start of the Wilson cycle at 3 Ga shown by diamonds from subcontinental mantle. *Science* **333**, 434–436 (2011).
17. R. J. Stern, Evidence from ophiolites, blueschists, and ultrahigh-pressure metamorphic terranes that the modern episode of subduction tectonics began in Neoproterozoic time. *Geology* **33**, 557–560 (2005).
18. M. J. Van Kranendonk, R. Hugh Smithies, A. H. Hickman, M. T. D. Wingate, S. Bodorkos, Evidence for mesoarchean (~3.2Ga) rifting of the pilbara craton: The missing link in an early precambrian wilson cycle. *Precambrian Res.* **177**, 145–161 (2010).
19. S. Turner, T. Rushmer, M. Reagan, J.-F. Moyen, Heading down early on? Start of subduction on Earth. *Geology* **42**, 139–142 (2014).
20. D. A. Evans, S. A. Pisarevsky, Plate tectonics on early Earth? Weighing the paleomagnetic evidence, in *When Did Plate Tectonics Begin on Planet Earth*, K. C. Condie, V. Pease, Eds. (Geological Society of America, 2008), vol. 440, pp. 249–263.
21. P. A. Cawood, A. Kroner, S. Pisarevsky, Precambrian plate tectonics: Criteria and evidence. *GSA Today* **16**, 4–10 (2006).
22. P. A. Cawood, C. J. Hawkesworth, S. A. Pisarevsky, B. Dhuime, F. A. Capitanio, O. Nebel, Geological archive of the onset of plate tectonics. *Philos. T. R. Soc. A* **376**, 20170405 (2018).
23. C. O'Neill, S. Turner, T. Rushmer, The inception of plate tectonics: A record of failure. *Phil. Trans. R. Soc. A.* **376**, 20170414 (2018).
24. K. J. Matthews, K. T. Maloney, S. Zahirovic, S. E. Williams, M. Seton, R. D. Müller, Global plate boundary evolution and kinematics since the late Paleozoic. *Global Planet. Change* **146**, 226–250 (2016).
25. J. J. Fuentes, J. W. Crowley, R. Dasgupta, J. X. Mitrovica, The influence of plate tectonic style on melt production and CO_2 outgassing flux at mid-ocean ridges. *Earth Planet. Sci. Lett.* **511**, 154–163 (2019).
26. A. Hickman, Pilbara Supergroup of the East Pilbara Terrane, Pilbara Craton: Updated lithostratigraphy and comments on the influence of vertical tectonics. *GSWA Annual Review* **10**, 50–59 (2009).
27. M. J. Van Kranendonk, H. R. Smithies, A. H. Hickman, D. C. Champion, Review: Secular tectonic evolution of Archean continental crust: Interplay between horizontal and vertical processes in the formation of the Pilbara Craton, Australia. *Terra Nova* **19**, 1–38 (2007).
28. M. J. Van Kranendonk, Geological Survey of Western Australia, *Revised Lithostratigraphy of Archean Supracrustal and Intrusive Rocks in the Northern Pilbara Craton, Western Australia* (Geological Survey of Western Australia, 2006).
29. M. J. Van Kranendonk, *Structural Geology of the Central Part of the Lalla Rookh Western Shaw Structural Corridor, Pilbara Craton, Western Australia* (Geological Survey of Western Australia, 2008).
30. M. J. Van Kranendonk, W. J. Collins, Timing and tectonic significance of Late Archaean, sinistral strike-slip deformation in the Central Pilbara Structural Corridor, Pilbara Craton, Western Australia. *Precambrian Research* **88**, 207–232 (1998).
31. M. J. Van Kranendonk, *Geology of the North Shaw 1: 100 000 Sheets: Sheets 2755* (Geological Survey of Western Australia, 2000).
32. B. Rasmussen, I. R. Fletcher, S. Sheppard, Isotopic dating of the migration of a low-grade metamorphic front during orogenesis. *Geology* **33**, 773–776 (2005).
33. P. A. Cawood, I. M. Tyler, Assembling and reactivating the Proterozoic Capricorn Orogen: Lithotectonic elements, orogenies, and significance. *Precambrian Res.* **128**, 201–218 (2004).
34. Z. X. Li, W. Guo, C. M. C. A. Powell, Timing and genesis of Hamersley BIF-hosted iron deposits: A new palaeomagnetic interpretation. MERIWA Project M242, (Minerals & Energy Research Institute of Western Australia, 2000), vol. 199.
35. G. Pullaiah, E. Irving, K. L. Buchan, D. J. Dunlop, Magnetization changes caused by burial and uplift. *Earth Planet. Sci. Lett.* **28**, 133–143 (1975).
36. L. Tauxe, G. S. Watson, The fold test: An eigen analysis approach. *Earth Planet. Sci. Lett.* **122**, 331–341 (1994).
37. G. Strik, T. S. Blake, T. E. Zegers, S. H. White, C. G. Langereis, Palaeomagnetism of flood basalts in the Pilbara Craton, Western Australia: Late Archaean continental drift and the oldest known reversal of the geomagnetic field. *J. Geophys. Res. Solid Earth* **108**, 2551 (2003).
38. D. Glenn, D. LeSage, R. Fu, B. Weiss, R. Walsworth, *APS Division of Atomic, Molecular and Optical Physics Meeting Abstracts* (2015), vol. 1, 1088 pp.
39. R. Huang, C.-T. Lin, W. Sun, X. Ding, W. Zhan, J. Zhu, The production of iron oxide during peridotite serpentinization: Influence of pyroxene. *Geosci. Front.* **8**, 1311–1321 (2017).
40. R. Day, M. Fuller, V. A. Schmidt, Hysteresis properties of titanomagnetites: Grain-size and compositional dependence. *Phys. Earth Planet. In.* **13**, 260–267 (1977).
41. D. J. Dunlop, Theory and application of the Day plot (M_{rs}/M_s versus H_{cr}/H_c) 1. Theoretical curves and tests using titanomagnetite data. *J. Geophys. Res. Solid Earth* **107**, EPM 4-1–EPM 4-22 (2002).
42. D. Wang, R. Van der Voo, D. R. Peacor, Low-temperature alteration and magnetic changes of variably altered pillow basalts. *Geophys. J. Int.* **164**, 25–35 (2006).
43. E. J. W. Verwey, Electronic conduction of magnetite (Fe_3O_4) and its transition point at low temperatures. *Nature* **144**, 327–328 (1939).
44. A. V. Smirnov, J. A. Tarduno, D. A. D. Evans, Evolving core conditions ca. 2 billion years ago detected by paleosecular variation. *Phys. Earth Planet. In.* **187**, 225–231 (2011).
45. M. W. McElhinny, P. L. McFadden, Palaeosecular variation over the past 5 Myr based on a new generalized database. *Geophys. J. Int.* **131**, 240–252 (1997).
46. M. W. McElhinny, W. E. Senanayake, Paleomagnetic evidence for the existence of the geomagnetic field 3.5 Ga ago. *J. Geophys. Res. Solid Earth* **85**, 3523–3528 (1980).
47. P. V. Doubrovine, T. Veikkolainen, L. J. Pesonen, E. Piispa, S. Ots, A. V. Smirnov, E. V. Kulakov, A. J. Biggin, Latitude dependence of geomagnetic paleosecular variation and its relation to the frequency of magnetic reversals: Observations from the cretaceous and jurassic. *Geochem. Geophys. Geosyst.* **20**, 1240–1279 (2019).
48. A. H. Saad, Paleomagnetism of Franciscan ultramafic rocks from Red Mountain, California. *J. Geophys. Res.* **74**, 6567–6578 (1969).
49. K. Bradley, B. P. Weiss, R. Buick, Records of geomagnetism, climate, and tectonics across a Paleoarchean erosion surface. *Earth Planet. Sci. Lett.* **419**, 1–13 (2015).
50. D. Evans, A. V. Smirnov, A. Gumsley, Paleomagnetism and U–Pb geochronology of the black range dykes, Pilbara Craton, Western Australia: A neoarchean crossing of the polar circle. *Aust. J. Earth Sci.* **64**, 225–237 (2017).
51. T. H. Torsvik, R. van der Voo, U. Preeden, C. Mac Niocaill, B. Steinberger, P. V. Doubrovine, D. J. J. van Hinsbergen, M. Domeier, C. Gaina, E. Tohver, J. G. Meert, P. J. A. McCausland, L. R. M. Cocks, Phanerozoic polar wander, palaeogeography and dynamics. *Earth-Sci. Rev.* **114**, 325–368 (2012).
52. C. O'Neill, A. Lenardic, L. Moresi, T. H. Torsvik, C.-T. A. Lee, Episodic Precambrian subduction. *Earth Planet. Sci. Lett.* **262**, 552–562 (2007).
53. V. C. Tsai, D. J. Stevenson, Theoretical constraints on true polar wander. *J. Geophys. Res. Solid Earth* **112**, B05415 (2007).
54. J. Creveling, J. Mitrovica, N.-H. Chan, K. Latychev, I. Matsuyama, Mechanisms for oscillatory true polar wander. *Nature* **491**, 244–248 (2012).
55. J. L. Kirschvink, The least-squares line and plane and the analysis of palaeomagnetic data. *Geophys. J. Roy. Astron. Soc.* **62**, 699–718 (1980).
56. D. R. Glenn, R. R. Fu, P. Kehayias, D. le Sage, E. A. Lima, B. P. Weiss, R. L. Walsworth, Micrometer-scale magnetic imaging of geological samples using a quantum diamond microscope. *Geochem. Geophys. Geosyst.* **18**, 3254–3267 (2017).
57. E. A. Lima, B. P. Weiss, Obtaining vector magnetic field maps from single-component measurements of geological samples. *J. Geophys. Res. Solid Earth* **114**, B06102 (2009).
58. R. R. Doell, Paleomagnetic secular variation study of lavas from the Massif central, France. *Earth Planet. Sci. Lett.* **8**, 352–362 (1970).
59. A. Cox, Latitude dependence of the angular dispersion of the geomagnetic field. *Geophys. J. Int.* **20**, 253–269 (1970).
60. N. D. Watkins, Brunhes epoch geomagnetic secular variation on Reunion Island. *J. Geophys. Res.* **78**, 7763–7768 (1973).
61. B. Efron, *The Jackknife, the Bootstrap, and Other Resampling Plans* (Siam, 1982), vol. 38.
62. C. Hawkesworth, P. Cawood, T. Kemp, C. Storey, B. Dhuime, Geochemistry. A matter of preservation. *Science* **323**, 49–50 (2009).

63. M. Pujol, B. Marty, R. Burgess, G. Turner, P. Philippot, Argon isotopic composition of Archaean atmosphere probes early Earth geodynamics. *Nature* **498**, 87–90 (2013).
64. L. D. Ashwal, G. M. Bybee, Crustal evolution and the temporality of anorthosites. *Earth-Sci. Rev.* **173**, 307–330 (2017).
65. M. E. Barley, B. Krapez, D. I. Groves, R. Kerrich, The Late Archaean bonanza: Metallogenic and environmental consequences of the interaction between mantle plumes, lithospheric tectonics and global cyclicity. *Precambrian Res.* **91**, 65–90 (1998).
66. S. Tappe, K. A. Smart, D. G. Pearson, A. Steenfelt, A. Simonetti, Craton formation in Late Archean subduction zones revealed by first Greenland eclogites. *Geology* **39**, 1103–1106 (2011).
67. D. Pearson, N. Wittig, The formation and evolution of cratonic mantle lithosphere–evidence from mantle xenoliths. *Treatise on Geochemistry* **2014**, 255–292 (2014).
68. N. S. C. Simon, R. W. Carlson, D. G. Pearson, G. R. Davies, The origin and evolution of the Kaapvaal cratonic lithospheric mantle. *J. Petrol.* **48**, 589–625 (2007).
69. R. H. Smithies, M. J. Van Kranendonk, D. C. Champion, The Mesoarchean emergence of modern-style subduction. *Gondw. Res.* **11**, 50–68 (2007).
70. R. H. Smithies, D. C. Champion, K. F. Cassidy, Formation of Earth's early Archaean continental crust. *Precambrian Res.* **127**, 89–101 (2003).
71. A. M. Bauer, C. M. Fisher, J. D. Vervoort, S. A. Bowring, Coupled zircon Lu–Hf and U–Pb isotopic analyses of the oldest terrestrial crust, the >4.03 Ga Acasta Gneiss Complex. *Earth Planet. Sci. Lett.* **458**, 37–48 (2017).
72. E. A. Bell, T. M. Harrison, M. T. McCulloch, E. D. Young, Early Archean crustal evolution of the Jack Hills Zircon source terrane inferred from Lu–Hf, $^{207}Pb/^{206}Pb$, and $\delta^{18}O$ systematics of Jack Hills zircons. *Geochim. Cosmochim. Acta* **75**, 4816–4829 (2011).
73. T. E. Zegers, D. R. Nelson, J. R. Wijbrans, S. H. White, SHRIMP U-Pb zircon dating of Archean core complex formation and pancratonic strike-slip deformation in the East Pilbara Granite-Greenstone Terrain. *Tectonics* **20**, 883–908 (2001).
74. A. Kloppenburg, S. H. White, T. E. Zegers, Structural evolution of the warrawoona greenstone belt and adjoining granitoid complexes, Pilbara Craton, Australia: Implications for archaean tectonic processes. *Precambrian Res.* **112**, 107–147 (2001).
75. M. Bickle, L. F. Bettenay, H. J. Chapman, D. I. Groves, N. J. McNaughton, I. H. Campbell, J. R. de Laeterd, Origin of the 3500-3300 Ma calc-alkaline rocks in the Pilbara Archaean: Isotopic and geochemical constraints from the Shaw Batholith. *Precambrian Res.* **60**, 117–149 (1993).
76. H. Furnes, M. de Wit, H. Staudigel, M. Rosing, K. Muehlenbachs, A vestige of Earth's oldest ophiolite. *Science* **315**, 1704–1707 (2007).
77. F. E. Jenner, V. C. Bennett, G. Yaxley, C. R. L. Friend, O. Nebel, Eoarchean within-plate basalts from southwest Greenland. *Geology* **41**, 327–330 (2013).
78. C. M. Fisher, J. D. Vervoort, Using the magmatic record to constrain the growth of continental crust—The Eoarchean zircon Hf record of Greenland. *Earth Planet. Sci. Lett.* **488**, 79–91 (2018).
79. P. Boehnke, E. A. Bell, T. Stephan, R. Trappitsch, C. B. Keller, O. S. Pardo, A. M. Davis, T. M. Harrison, M. J. Pellin, Potassic, high-silica Hadean crust. *Proc. Natl. Acad. Sci. U.S.A.* **115**, 6353–6356 (2018).
80. O. Laurent, H. Martin, J. F. Moyen, R. Doucelance, The diversity and evolution of late-Archean granitoids: Evidence for the onset of "modern-style" plate tectonics between 3.0 and 2.5 Ga. *Lithos* **205**, 208–235 (2014).
81. P. W. Schmidt, B. J. J. Embleton, Prefolding and overprint magnetic signatures in Precambrian (~ 2.9–2.7 Ga) igneous rocks from the Pilbara Craton and Hamersley Basin, NW Australia. *J. Geophys. Res. Solid Earth* **90**, 2967–2984 (1985).
82. P. W. Schmidt, D. A. Clark, Palaeomagnetism and magnetic anisotropy of Proterozoic banded-iron formations and iron ores of the Hamersley Basin, Western Australia. *Precambrian Res.* **69**, 133–155 (1994).
83. Y. Suganuma, Y. Hamano, S. Niitsuma, M. Hoashi, T. Hisamitso, N. Niitsuma, K. Kodama, M. Nedachi, Paleomagnetism of the Marble Bar Chert Member, Western Australia: Implications for apparent polar wander path for Pilbara craton during Archean time. *Earth Planet. Sci. Lett.* **252**, 360–371 (2006).
84. M. T. D. Wingate, in *A Palaeomagnetic Test of the Kaapvaal - Pilbara (Vaalbara) Connection at 2.78 Ga*. (1998), vol. 101, pp. 257–274.
85. S. Denyszyn, J. Feinberg, P. R. Renne, G. R. Scott, in *Revisiting the Age and Paleomagnetism of the Modipe Gabbro of South Africa*. (2013), vol. 238, pp. 176–185.
86. M. O. de Kock, D. A. D. Evans, N. J. Beukes, Validating the existence of Vaalbara in the Neoarchean. *Precambrian Res.* **174**, 145–154 (2009).
87. G. Strik, M. J. De Wit, C. G. Langereis, Palaeomagnetism of the neoarchaean pongola and ventersdorp supergroups and an appraisal of the 3.0–1.9 Ga apparent polar wander path of the Kaapvaal Craton, Southern Africa. *Precambrian Res.* **153**, 96–115 (2007).
88. A. J. Biggin, M. J. de Wit, C. G. Langereis, T. E. Zegers, S. Voûte, M. J. Dekkers, K. Drost, Palaeomagnetism of Archaean rocks of the Onverwacht Group, Barberton Greenstone Belt (southern Africa): Evidence for a stable and potentially reversing geomagnetic field at ca. 3.5 Ga. *Earth Planet. Sci. Lett.* **302**, 314–328 (2011).
89. Y. Usui, J. A. Tarduno, M. Watkeys, A. Hofmann, R. D. Cottrell, Evidence for a 3.45-billion-year-old magnetic remanence: Hints of an ancient geodynamo from conglomerates of South Africa. *Geochem. Geophys. Geosyst.* **10**, Q09Z07 (2009).
90. A. Yoshihara, Y. Hamano, Paleomagnetic constraints on the Archean geomagnetic field intensity obtained from komatiites of the Barberton and Belingwe greenstone belts, South Africa and Zimbabwe. *Precambrian Res.* **131**, 111–142 (2004).
91. T. E. Zegers, M. J. de Wit, J. Dann, S. H. White, Vaalbara, Earth's oldest assembled continent? A combined structural, geochronological, and palaeomagnetic test. *Terra Nova* **10**, 250–259 (1998).
92. E. Cheney, in *Extended Abstracts Geocongress*. (1990), vol. 90, pp. 88–91.
93. P. W. Schmidt, A review of precambrian palaeomagnetism of Australia: Palaeogeography, supercontinents, glaciations and true polar wander. *Gondw. Res.* **25**, 1164–1185 (2014).
94. A. H. Hickman, *Northwest Pilbara Craton: A Record of 450 Million Years in the Growth of Archean Continental Crust* (Report no. 160, Geological Survey of Western Australia, East Perth, Western Australia, 2016), 104 p.
95. P. W. Layer, A. Kröner, M. McWilliams, An archean geomagnetic reversal in the Kaap Valley Pluton, South Africa. *Science* **273**, 943–946 (1996).
96. P. W. Layer, M. Lopez-Martinez, A. Kröner, D. York, M. McWilliams, Thermochronometry and palaeomagnetism of the Archaean Nelshoogte Pluton, South Africa. *Geophys. J. Int.* **135**, 129–145 (1998).
97. J. A. Tarduno, R. D. Cottrell, M. K. Watkeys, D. Bauch, Geomagnetic field strength 3.2 billion years ago recorded by single silicate crystals. *Nature* **446**, 657–660 (2007).
98. S. Letts, T. H. Torsvik, S. J. Webb, L. D. Ashwal, Palaeomagnetism of the 2054 Ma Bushveld Complex (South Africa): Implications for emplacement and cooling. *Geophys. J. Int.* **179**, 850–872 (2009).
99. J. R. Lowrey, D. A. Wyman, T. J. Ivanic, M. P. Roberts, Platy Pyroxene: New insights into spinifex texture. *J. Petrol.* **58**, 1671–1700 (2017).
100. S. Bouquain, N. T. Arndt, E. Hellebrand, F. Faure, Crystallochemistry and origin of pyroxenes in komatiites. *Contrib. Mineral. Petrol.* **158**, 599 (2009).
101. M. T. Wingate, J. W. Giddings, Age and palaeomagnetism of the Mundine Well dyke swarm, Western Australia: Implications for an Australia–Laurentia connection at 755 Ma. *Precambrian Res.* **100**, 335–357 (2000).

Acknowledgments: We thank C. Moore and T. Kilian for assistance in the field. We thank K. Bristol for help with rock-magnetic experiments. We also thank A. Hickman and M. V. Kranendonk for their insights into the field areas from which we sampled and the Pilbara more generally, as well as K. Bradley for consultation on previous paleomagnetic results in the Pilbara. We thank B. Weiss for the use of his rock magnetometer and the MIT Paleomagnetism Laboratory. We thank R. Fisher, M. Brennan, and J. Dong for the use of the Raman microscope in the Harvard Mineral Physics Laboratory. **Funding:** This work was supported by grants from the National Science Foundation (EAR-1847042, EAR-1723023, and EAR-0711453). **Author contributions:** A.R.B. led the study with interpretive and analytical contributions from all authors, most notably R.R.F., who played a supervisory role. D.A.D.E., A.V.S., and I.R.R. participated in an early field sampling campaign in the ESGB (I.R.R. performed laboratory measurements at Yale) and contributed to the data analysis and interpretations. A.R.B. and R.R.F. conducted field sampling (A.R.B. performed laboratory measurements at MIT) in the SVS. **Competing interests:** The authors declare that they have no competing interests. **Data and materials availability:** All data needed to evaluate the conclusions in the paper are present in the paper and/or the Supplementary Materials. The data will also be available through the Magnetics Information Consortium (MagIC) Database (www2.earthref.org/MagIC).

Submitted 15 October 2019
Accepted 30 January 2020
Published 22 April 2020
10.1126/sciadv.aaz8670

Citation: A. R. Brenner, R. R. Fu, D. A. D. Evans, A. V. Smirnov, R. Trubko, I. R. Rose, Paleomagnetic evidence for modern-like plate motion velocities at 3.2 Ga. *Sci. Adv.* **6**, eaaz8670 (2020).

Paleomagnetic evidence for modern-like plate motion velocities at 3.2 Ga

Alec R. Brenner, Roger R. Fu, David A.D. Evans, Aleksey V. Smirnov, Raisa Trubko and Ian R. Rose

Sci Adv **6** (17), eaaz8670.
DOI: 10.1126/sciadv.aaz8670

Science Advances
AAAS

advances.sciencemag.org/cgi/content/full/6/17/eaaz8670/DC1

Supplementary Materials for

Paleomagnetic evidence for modern-like plate motion velocities at 3.2 Ga

Alec R. Brenner*, Roger R. Fu, David A.D. Evans, Aleksey V. Smirnov, Raisa Trubko, Ian R. Rose

*Corresponding author. Email: alecbrenner@g.harvard.edu

Published 22 April 2020, *Sci. Adv.* **6**, eaaz8670 (2020)
DOI: 10.1126/sciadv.aaz8670

The PDF file includes:

Other Supplementary Material for this manuscript includes the following:

(available at advances.sciencemag.org/cgi/content/full/6/17/eaaz8670/DC1)

Supplementary Materials

Proposed ages for the initiation of modern style plate tectonics referenced in Fig. 5A

A. Before 0.7-0.8 Ga based on the global record of high-pressure metamorphic rocks (*17*);
B. After 2.6 Ga based on global detrital zircon age peaks (*62*);
C. Before 2.7 Ga based on Ar composition of the atmosphere (*63*), global records of anorthosite complexes (*64*) and metallogenic patterns (*65*), and paleomagnetic pole comparisons (*20-23*);
D. At approximately 3.0 Ga based on Re-Os systematics of mantle xenoliths and eclogites (*66-68*), global Hf and O isotope records in zircons (*14*), geochemical sampling of shales and diamictites (*3*), and eclogitic inclusions in diamonds (*16*) in multiple cratons;
E. At approximately 3.1-3.2 Ga based on mapping arc-like (*69, 70*) and rift-like (*18, 27*) sequences in the Pilbara Craton, Western Australia;
F. Before 3.5-3.6 Ga based on the global record of Ti isotopes in shales (*4*), isotope systematics of gneisses in the Slave Craton, Canada (*71*) inclusions in Hadean zircons from the Yilgarn Craton, Western Australia (*72*), and subhorizontal tectonic structures (*73, 74*) and arc-like granitoids from the Pilbara Craton (*75*);
G. Before 3.7 Ga based on field mapping of putative ophiolites in the Isua Greenstone Belt, Greenland (*76*);
H. Before 3.8 Ga based on trace element systematics and stratigraphy of arc-like rocks in the Isua Greenstone Belt (*77, 78*) and the Nuvvuagittuq Greenstone Belt, Canada (*19*);
I. Before 4.2 Ga based on zircon inclusions from the Nuvvuagittuq Greenstone Belt (*79*).

Another possibility is that of an episodic, local or gradual transition to a mobile-lid (*10, 52*). It is argued in this framework that plate tectonics appeared in some areas before others (*80*).

Archean paleogeography of the East Pilbara and Kaapvaal cratons

Robust Neoarchean poles demonstrating sustained latitudinal motion have been measured from the 2772-2715 Ma Fortescue Group large igneous province, which includes extrusive packages numbered P0-P10 and the 2772±2 Ma Black Ranges Dike (pole BRS) (*37, 50, 81*). The resulting >2772 to <2715 Ma APW path traces a high-latitude arc with high implied plate paleovelocities of up to tens of degrees per My (*37*) and is followed by a group of ~1700 Ma overprint directions from late Archean to Paleoproterozoic rocks (*34, 82*).

The youngest paleomagnetic pole among those of Paleoarchean age is based on the ~3350-3335 Ma Euro Basalt (EBm), which was sampled by the Archean Biosphere Drilling Project 8 (ABDP-8) drill core (*49*). The EBm pole, interpreted to be a chemical remanent magnetization (CRM) acquired during early hydrothermal seafloor alteration at ~3350 Ma, is likely free from azimuthal misorientation of the core because physical alignment of the core fragments was possible for the ~300 m depth of the drill core from which the paleomagnetic data was taken (*49*). However, the similarity of the reversed EBm direction to that of ~2715 Ma overprints from the upper Fortescue Group (*37*) raises the possibility of an overprint origin. The drill core provenance of EBm samples precludes the application of rigorous paleomagnetic field tests to confirm the primary origin of its magnetization. Despite this concern, we consider an early post-emplacement CRM origin of EBm the most probable interpretation based on its low metamorphic grade and the lack of Fortescue age overprints in adjacent rock units, including basalts of the lower Fortescue Group (e.g., P0) (*37*).

In addition to the EBm pole, Bradley, Weiss and Buick (*49*) report a paleopole (CDm) from the Coucal and Double Bar Formations, which they argue is a primary record of a shortly post-emplacement CRM. This is supported by rock magnetic signatures of an oxidative weathering profile across the overlying unconformity and >3350 Ma Strelley Pool Chert. However, the poor precision of this pole's ~3515-3350 Ma age constraint hampers further analysis.

Seven stratigraphically-adjacent poles (MB1-7) have been reported from the 3476-3456 Ma Marble Bar Chert based on samples from the ABDP-1 drill core (*83*). These data appeared to suggest high latitudinal drift speeds of 12-112 cm/yr during the deposition of the Marble Bar Chert. However, stable remanence directions are best fit by a small circle centered on the drill core drill core, strongly suggesting sample misorientation as the cause of the purported polar motion (see the supplement of Bradley, Weiss and Buick (*49*)).

The oldest well-dated East Pilbara paleopole is from dacites and basalts of the 3471-3464 Ma Duffer Formation (DFM) (*46*). The pole is supported by a fold test (n=11 sites), albeit with two different greenstone belts serving as the "limbs" of the fold test. Although the potential exists for miscorrelation between the two greenstone belts, the chance alignment of the two tilt-corrected directions in such a scenario remains unlikely. While overprints may explain some of the directions used in the DFM pole (*49*), we consider it reliable.

Based on its two best-dated and most reliable Paleoarchean poles, DFM and EBm, the East Pilbara appears to have occupied relatively low latitudes between 3471-3464 Ma and 3350-3335 Ma. During this interval, the East Pilbara experienced latitudinal drift of ≥0.89±0.80 cm/y. While this drift rate is statistically resolvable from zero, it is low and may be consistent with either mobile-lid or stagnant-lid settings. This rate cannot unequivocally support uniformitarian tectonics between 3.47 and 3.35 Ga, and shows some consilience to the idea of a "stagnant lid" regime during this time.

South Africa's Kaapvaal craton has thus far provided the only other paleomagnetic results of similar antiquity. The most reliable paleolatitudes to date are those from the Neoarchean Ventersdorp Supergroup (*84-87*) and the Paleoarchean rocks of the Barberton Greenstone Belt (*88-90*). The similar APW paths of the Pilbara and Kaapvaal Cratons, from low-latitudes in the Paleoarchean to mid- and high-latitudes in the Neoarchean, have been used to argue for the existence and geometry of an Archean composite craton termed "Vaalbara" (*37, 86, 88, 91, 92*). Regardless of the veracity of the Vaalbara hypothesis, there is heretofore no unambiguous paleomagnetic evidence in either craton for fast latitudinal drift until after ~2.8 Ga.

While Mesoarchean paleopoles have been reported from both the Pilbara and Kaapvaal cratons, none thus far have been sufficiently characterized to permit calculation of precisely dated paleolatitudes, and are considered herein to be unreliable. One commonly cited pole in the paleomagnetic literature (e.g., Schmidt (*93*)) is that of the Mesoarchean "Millindinna Complex" (*82*) from the East Pilbara. Van Kranendonk, Smithies, Hickman and Champion (*27*) summarized the ages of pre-Fortescue intrusive suites throughout the Pilbara. "Millindinna" locality M1 (*82*) is from the Sherlock layered intrusion, part of the 2925 Ma Radley Suite of layered mafic-ultramafic complexes. The tabulated and mapped coordinates of "Millindinna" locality M2 are inconsistent in Schmidt and Embleton (*81*), but M2 is likely in what is now recognized as the Andover intrusion south of Roebourne municipality. That intrusion is suggested to be part of the 3015 Ma Orpheus Suite, or perhaps even older (*94*). The ≥90 My discrepancy in igneous crystallization ages between localities M1 and M2 provides an explanation for why their paleomagnetic directions are not parallel, and invalidates the allegedly positive fold test between them. It is conceivable that either or both localities record primary magnetizations, but further study is warranted.

In the Kaapvaal craton, Layer, Kröner and McWilliams (*95*) reported a series of paleopoles from the ~3220 Ma Kaap Valley Pluton, and argued that the approximate antipodality of several of these directions constitutes a record of Mesoarchean geomagnetic reversals. While provocative, this result has since been largely discredited. The lack of any paleohorizontal datum in the sampled rocks – which are often strongly sheared in their sampling sites at the margins of the pluton – severely limits their utility for paleolatitudinal reconstructions. Similar concerns apply to several additional results on Mesoarchean plutons from the Kaapvaal craton (*96, 97*). Additionally, the antipodal directions reported in this study have since been attributed to overprints from the ~2050 Ma Bushveld Complex to the northwest (*98*). The presence of both polarity magnetizations in an overprinting component casts strong doubt on the robustness of the reversal test used to argue for a primary origin for the high temperature remanence.

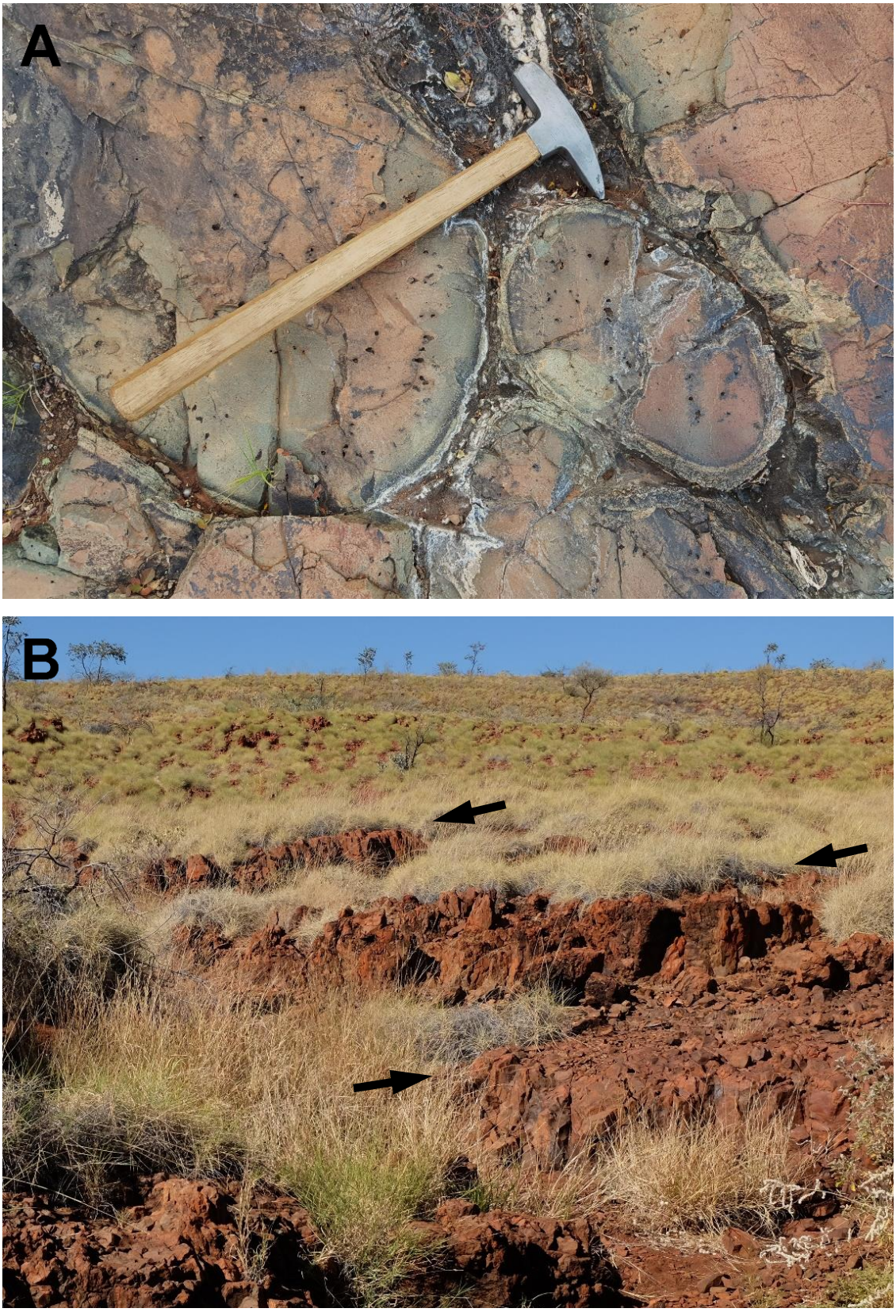

Fig. S1. Outcrop photographs of the Honeyeater Basalt. (**A**) Stream-cut exposure of relatively fresh pillows at area SVE, showing well-preserved vesicles, chilled margins, and altered intra-pillow hyaloclastite. Hammer is 47 cm long. Photo credit: Alec Brenner, Harvard University. (**B**) Three massive basalt flows exposed as subhorizontal terraces at area SVA. Arrows denote flow tops. For scale, the middle flow is ~1 m thick. Photo credit: Roger Fu, Harvard University.

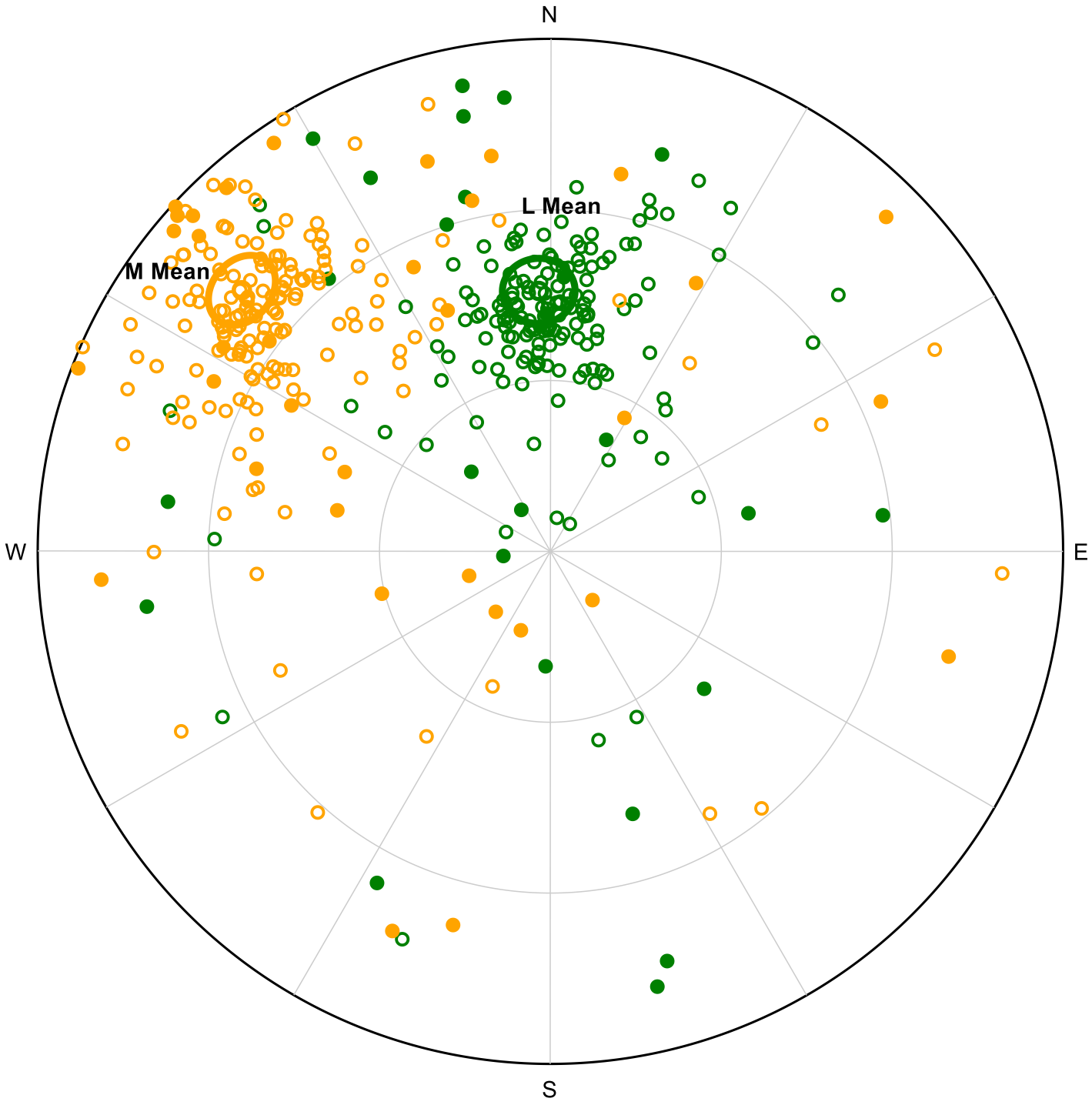

Fig. S2. L and M component directions. Equal-angle stereonet shows all measured L (green) and M (orange) component directions in *in situ* coordinates. Mean directions are points with error circles; individual fits are small points. Open points are upper hemisphere directions; filled points are lower hemisphere directions.

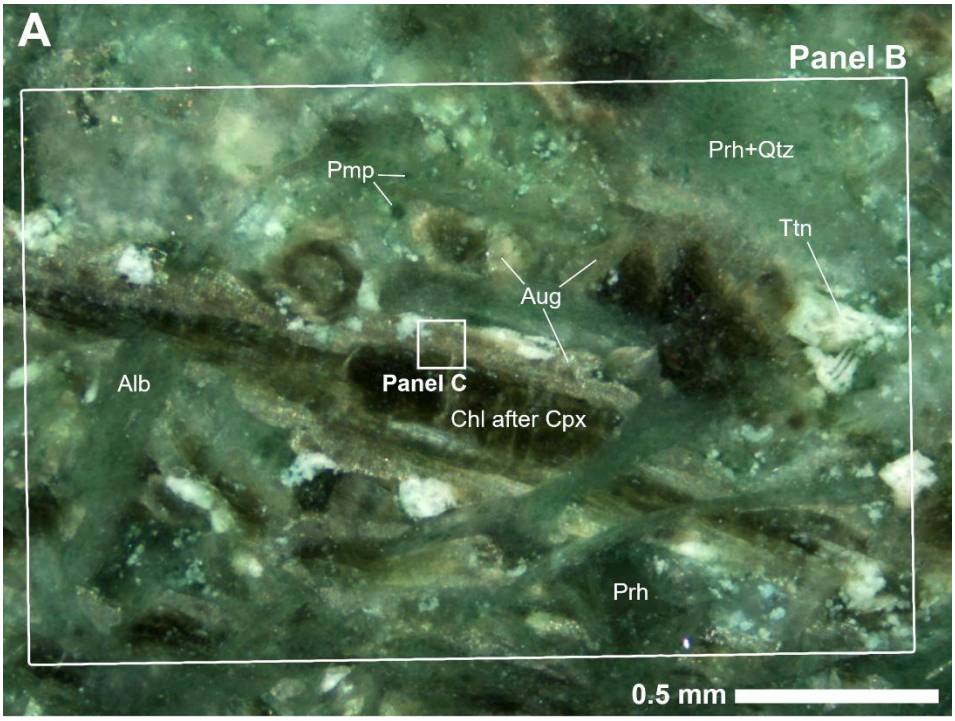

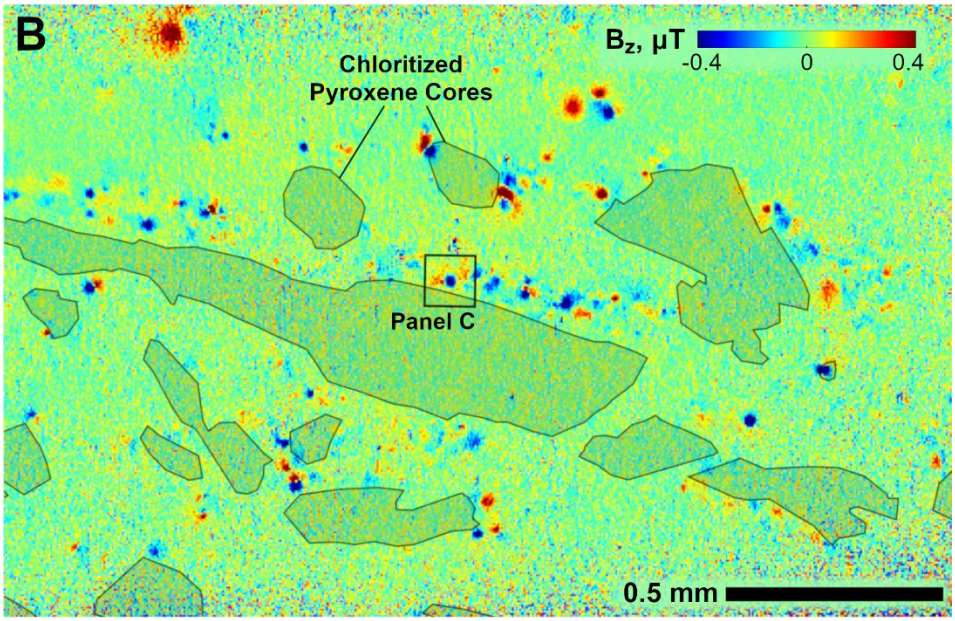

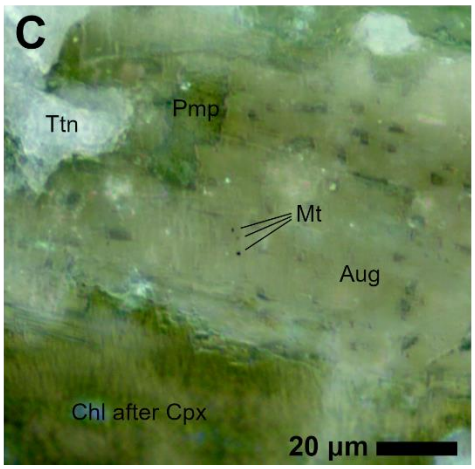

Fig. S3. Micromagnetic imaging and context of ferromagnetic carriers. (**A**) Cross-polarized optical image and (**B**) QDM micromagnetic map of NRM in a 1.5 mm thick section from sample SVD14. Magnetic sources correspond to regions of high field intensity (red and blue colors) and are localized to the rims of several-mm laths of augite (Aug) with chloritized zones of chamosite most likely after pigeonite (Chl after Cpx), suggesting thermochemical remagnetization shortly after emplacement. The augite rims and chloritized cores are remnants of zoned pigeonite-augite grains, a "pyroxene-spinifex" texture observed commonly in low-Mg komatiites (*99, 100*). Groundmass surrounding the laths is predominantly albite (Alb), titanite (Ttn) pseudomorphs most likely after ilmenite, and fine-grained intergrowths of prehnite (Prh), pumpellyite (Pmp), chlorite and quartz (Qtz), with accessory pyrite, phlogopite and sphalerite. **(C)** Magnified cross-polarized optical view centered on a magnetic source, revealing several- to sub-μm opaque grains, likely of magnetite (Mt).

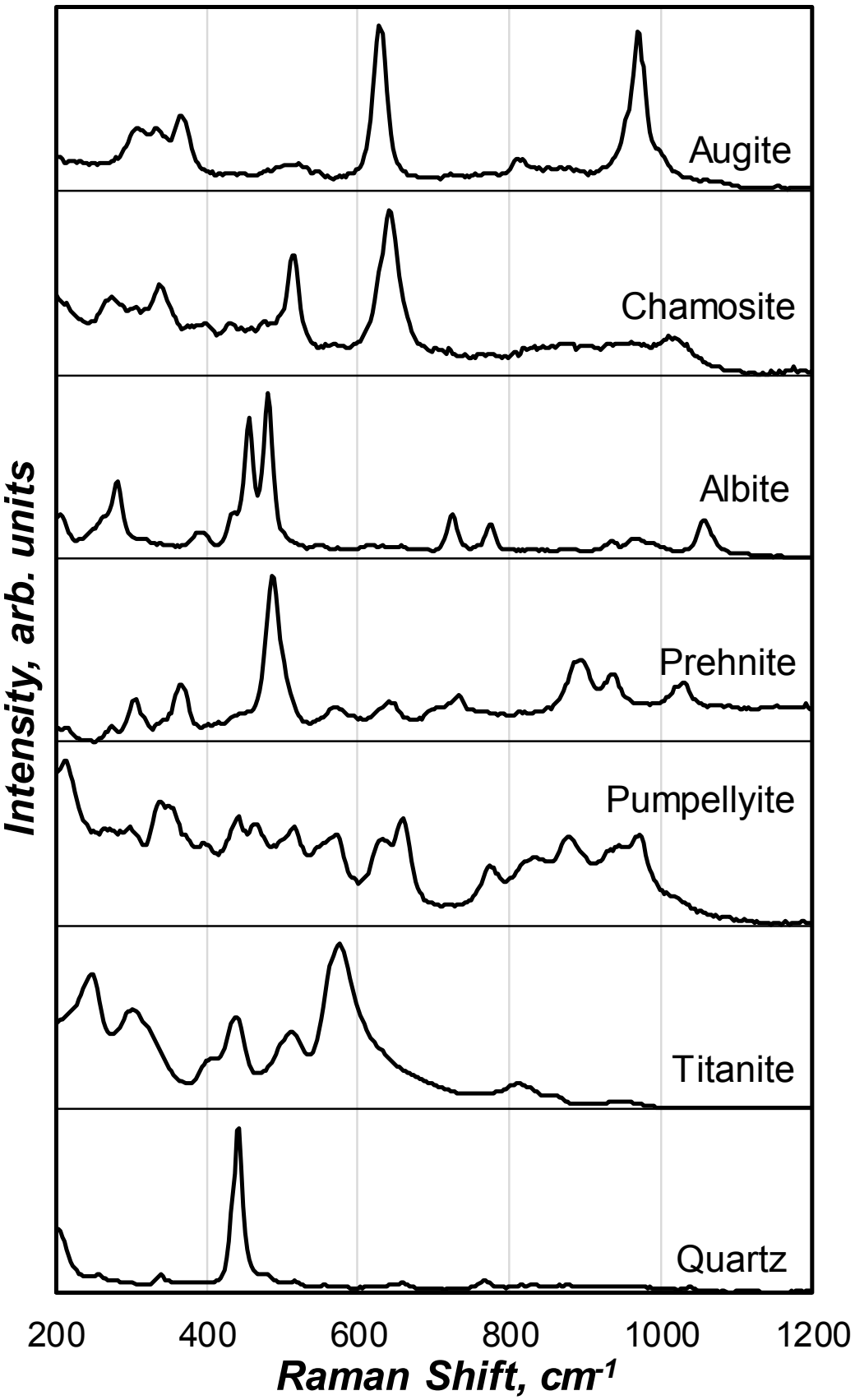

Fig. S4. Raman spectra of major phases observed with the QDM. The observed mineralogy is consistent with upper prehnite-pumpellyite to lower greenschist facies metamorphism in komatiitic basalts. The excitation wavelength is 532 nm for all spectra.

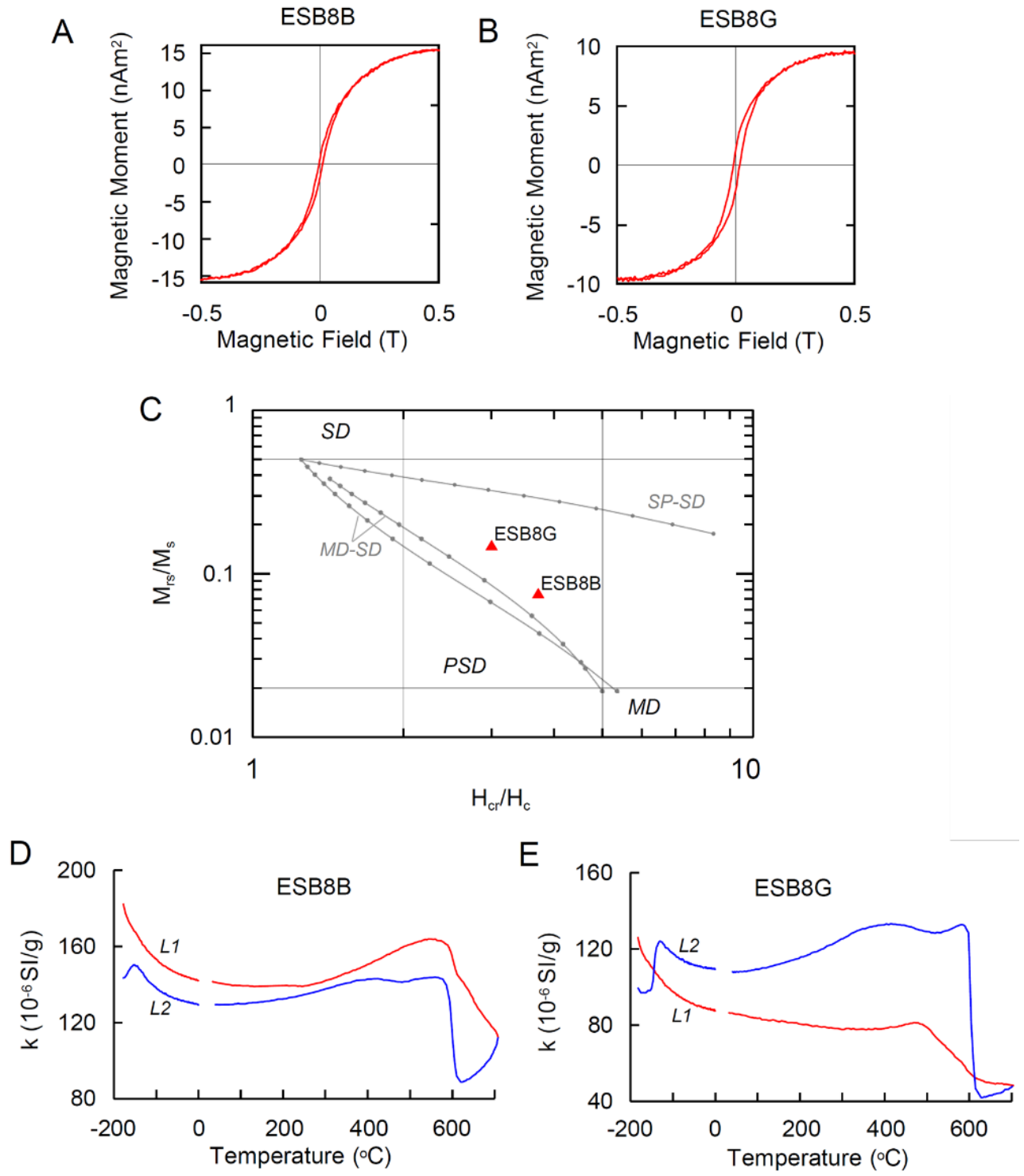

Fig. S5. Rock magnetic data from samples ESB8B and ESB8G. (**A, B**) Magnetic hysteresis loops after paramagnetic slope correction. (**C**) Magnetic hysteresis ratios (red triangles) plotted on a Day diagram (*40*). Grey lines are theoretical curves for mixtures of MD and SD grains (MD-SD lines, based on two different datasets), and SP (10 nm in size) and SD grains (SD-SP line) after Dunlop (*41*). Both samples plot in the region consistent with PSD magnetite. Abbreviations: H_c - coercivity; H_{cr} - coercivity of remanence; M_{rs} - saturation remanence; M_s - saturation magnetization; SD - single domain; PSD - pseudo-single domain; MD - multidomain. (**D, E**) Temperature dependencies of low-temperature magnetic susceptibility k(T) during initial heating (red curves) and subsequent cooling (blue curves). L1 and L2 show the low temperature k(T) runs before and after high-temperature run up to 700˚C, respectively.

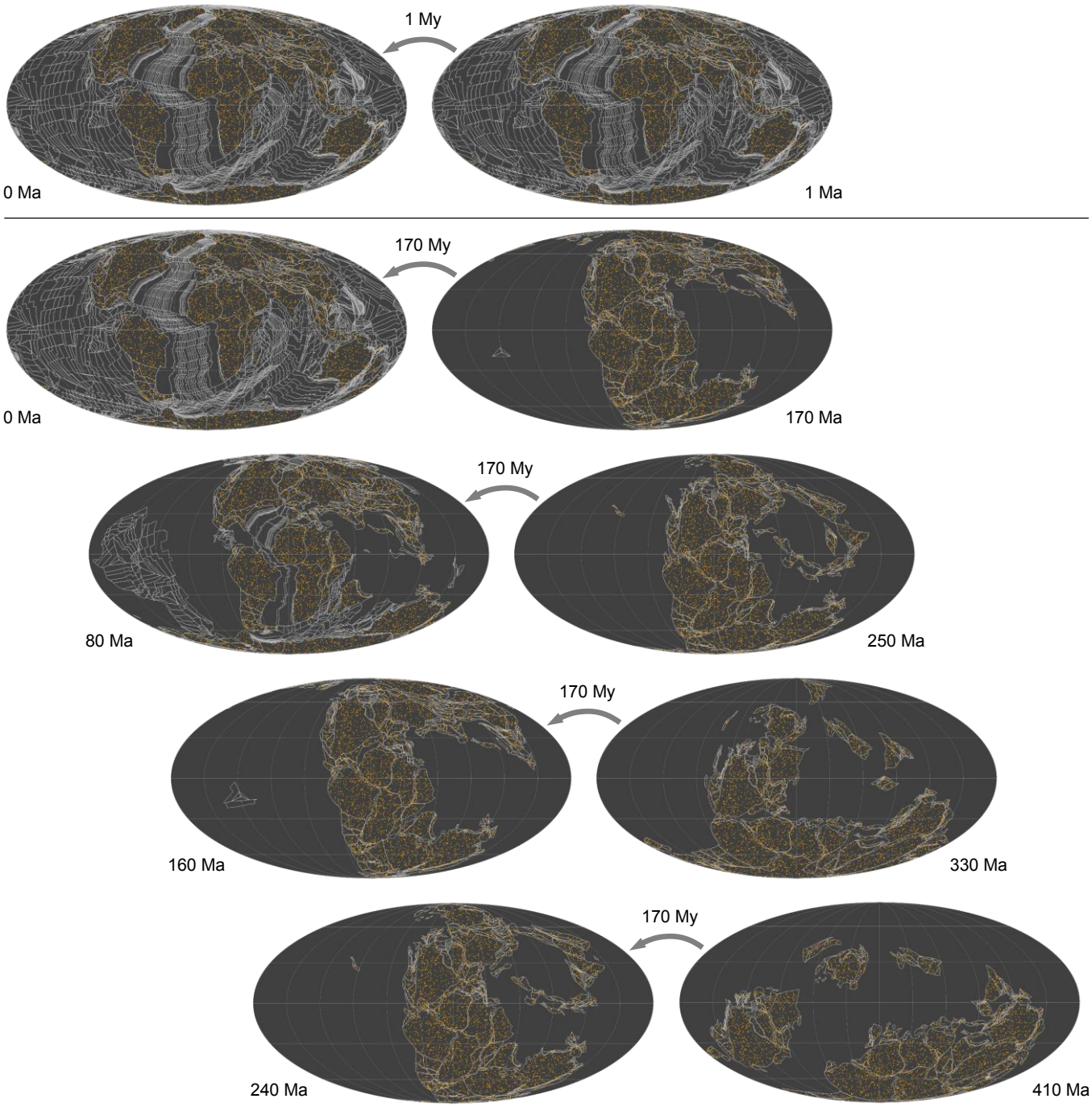

Fig. S6. Sampling of geologically-recent plate motions. The top left map shows N=3736 randomly selected points (orange) on the continents used to estimate distributions in Fig. 5b, anchored to plates (white outlines) on the modern Earth. The top right map shows the same points displaced to their reconstructed positions at 1 Ma according to the plate motion reconstruction of Matthews, Maloney, Zahirovic, Williams, Seton and Mueller (*24*), effectively producing a snapshot of recent instantaneous plate motion. All four rows below show the same points reconstructed to intervals that each bracket a 170 My interval of the last Wilson cycle. These intervals strongly time-average geologically recent plate motions, and are analogous to the ~170 My sampling interval between the Euro Basalt and Honeyeater Basalt in the Pilbara.

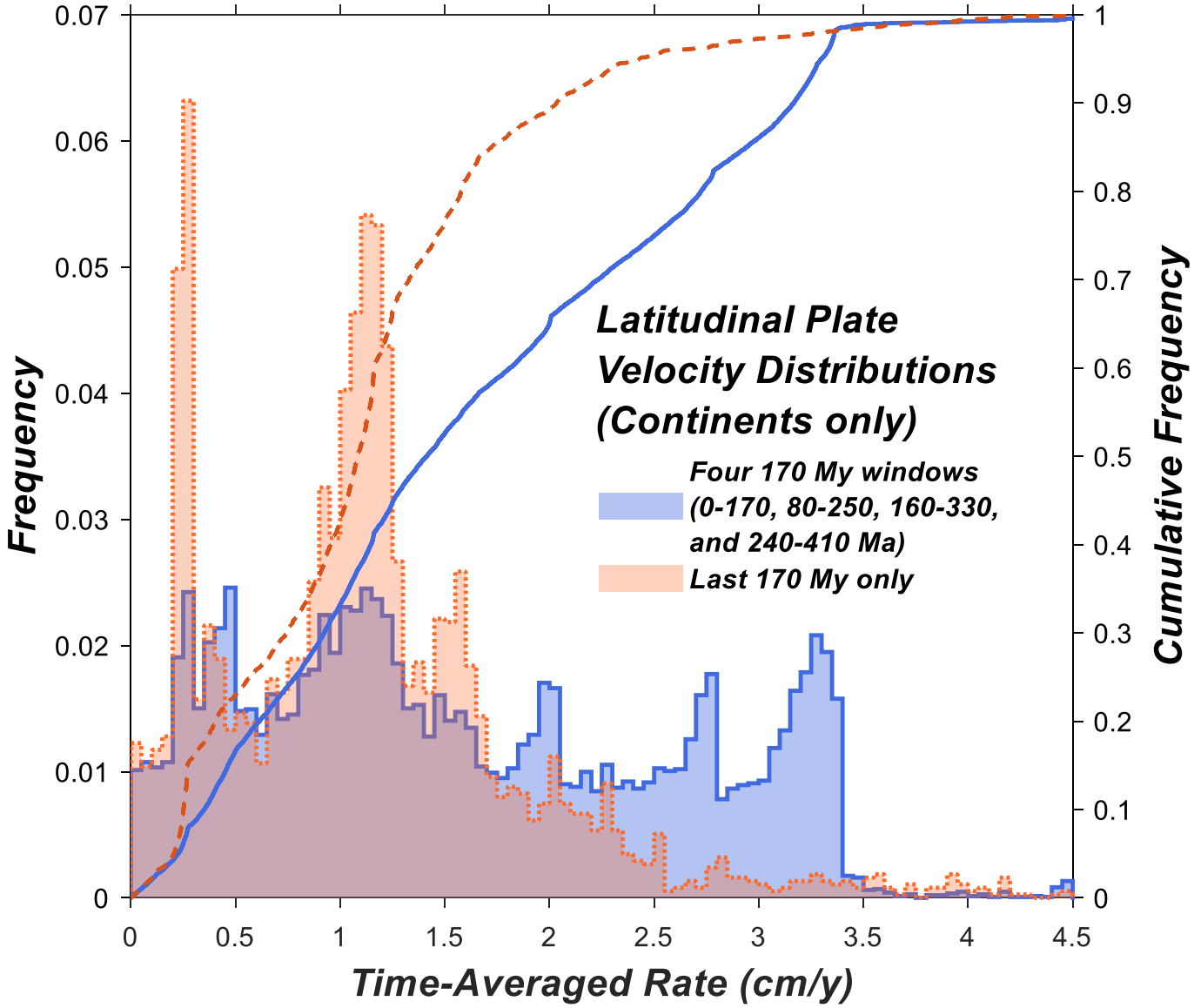

Fig. S7. Different 170 My time-averaged plate motion rate distributions. Distributions of time-averaged latitudinal velocities on the continents (*24*) recorded at N=3736 randomly selected points over four 170 Ma windows throughout the Phanerozoic (blue with solid lines) and from the present to 170 Ma (orange with dashed lines) and as both histograms and CDFs (line overlays). The distribution over only the last 170 My favors slower rates than does the four-interval distribution, since the las 170 My has been dominated by longitudinal motion of the continents during Pangaea breakup. By comparison, the four-interval distribution samples rates from all phases of the last Wilson cycle, and as such we use this less-biased distribution for comparison with Archean plate motion rates.

Table S1. H component directions by site and locality. Mean directions for each measured component are also reported (bottom). Subscript "geo" indicates geographic (*in situ*) coordinates; "tc" indicates tilt-corrected (stratigraphic) coordinates. Bedding attitudes, D, I, and α_{95} all in degrees. n/N gives the number of samples (or sites) used / number of samples (or sites) measured. Of the three possible H component mean directions given below, we consider the mean of areas SVA, SVC, SVD, and SVE the preferred mean direction. Localities SVB and ESA are not included due to absent or scattered H components. Tilt correction includes correction for the plunge of the 069°/41° fold axis of the SVS, except for in locality ESB. For

Locality	Site	Bedding	*n/N*	Used for Preferred H Mean	D_{geo}	I_{geo}	D_{tc}	I_{tc}	*R*	*K*	α_{95}
SVA	**0**	058/05	4/6	✓	232.5	84.2	192.6	82.0	3.98	156.0	7.4
	1	058/05	2/5	✓	54.6	79.9	79.4	79.0	1.96	23.1	54.6
	2	058/05	5/5	✓	238.4	81.7	205.8	80.3	4.89	35.1	13.1
	3	058/05	1/5		206.0	57.3	198.1	54.4	1.00	-	-
	4	058/05	0/5		-	-	-	-	-	-	-
	Mean	**058/05**	**3/5**		**239.3**	**88.6**	**160.6**	**84.9**	**2.97**	**65.4**	**15.4**
SVC	**1**	070/64	2/6		299.1	25.82	214.6	53.4	1.925	13.34	74.93
	3	070/64	5/6	✓	280.9	26.8	208.7	37.5	4.92	48.1	11.1
	4	070/64	2/5	✓	275.6	33.7	199.1	34.5	1.99	84.8	27.5
	5	070/64	2/6	✓	307.3	31.26	205.5	60.91	1.963	27.17	49.92
	6	070/64	0/5		-	-	-	-	-	-	-
	7	070/64	0/5		-	-	-	-	-	-	-
	Mean	**070/64**	**3/6**		**287.8**	**31.3**	**228.4**	**46.5**	**2.93**	**29.7**	**23.0**
SVD	**1**	125/25	3/5	✓	225.9	66.6	215.1	41.8	3.00	767.1	4.5
	2	125/25	2/5	✓	186.6	77.6	199.4	53.7	2.00	268.7	15.3
	3	125/25	5/5	✓	167.1	64.7	183.0	44.3	4.76	16.8	19.2
	Mean	**125/25**	**3/3**		**193.3**	**71.6**	**204.3**	**47.3**	**2.95**	**39.4**	**19.9**
SVE	**1**	058/30	2/5	✓	274.7	47.6	224.9	57.2	1.96	27.67	49.43
	2	058/30	2/6	✓	268.2	64.9	190.7	63.0	1.96	22.68	55.14
	3	058/30	4/6	✓	268.6	44.0	224.2	51.7	3.82	17.0	23.0
	4	058/30	0/5		-	-	-	-	-	-	-
	Mean	**058/30**	**3/4**		**270.8**	**52.2**	**225.6**	**59.2**	**2.96**	**50.5**	**17.5**
ESB	**7**	335/43	0/8		-	-	-	-	-	-	-
	8	335/43	7/8		230.5	43.2	168.7	76.6	6.92	76.5	6.9
	9	335/43	3/8		199.7	18.06	177.6	40.39	2.873	15.74	32.17
	10	335/43	0/8		-	-	-	-	-	-	-
	11	335/43	0/8		-	-	-	-	-	-	-
	13	335/43	0/9		-	-	-	-	-	-	-
	Mean	**335/43**	**2/6**		**213.0**	**31.5**	**175.5**	**58.5**	**1.90**	**10.1**	**89.1**
SVC/D/E H Mean		-	9/24		-	-	205.5	50.2	8.77	35.2	8.8
SVA/C/D/E (Preferred) H Mean		**-**	**12/24**		**-**	**-**	**203.7**	**59.0**	**11.30**	**15.8**	**11.3**
All Areas H Mean		-	14/24		-	-	199.7	59.4	13.15	15.3	10.5
M Mean		**-**	**198/-**		**310.3**	**-19.0**	**-**	**-**	**156.6**	**4.8**	**5.2**
L Mean		**-**	**181/-**		**357.4**	**-44.2**	**-**	**-**	**139.6**	**4.3**	**5.7**
AF Mean		**-**	**225/-**		**2.4**	**-37.8**	**-**	**-**	**76.7**	**1.5**	**13.1**

Table S2. H component VGPs and poles. Site VGPs are non-bold and locality mean poles are bold, with mean poles for H components across multiple localities at the bottom (our preferred pole is "HEBh"). Subscript "geo" indicates geographic (*in situ*) coordinates; "tc" indicates tilt-corrected (stratigraphic) coordinates. α_{95} in degrees; λ in degrees N; Φ in degrees E. The M component mean pole across all areas is also given ("HEBm") along with the semimajor/semiminor axes of its error ellipse, since its VGPs are not site-specific. Localities SVB and ESA are not included due to absent or scattered H components. Tilt correction includes correction for the plunge of the 069°/41° fold axis of the SVS, except for in locality ESB.

Locality	Site	Used for Preferred H Mean	λ_{geo}	Φ_{geo}	$\alpha_{95,\,geo}$	λ_{tc}	Φ_{tc}	$\alpha_{95,\,tc}$
SVA	**0**	✓	-28.2	108.8	-	-36.8	114.9	-
	1	✓	-9.4	135.3	-	-16.2	141.0	-
	2	✓	-29.2	103.2	-	-38.1	108.9	-
	Mean		**-22.9**	**116.5**	**30.6**	**-31.2**	**122.8**	**30.3**
SVC	**3**	✓	4.6	46.4	-	-63.3	33.6	-
	4	✓	-1.7	48.3	-	-71.9	384.7	-
	5	✓	25.7	61.5	-	-60.4	78.8	-
	Mean		**9.6**	**51.7**	**25.4**	**-67.1**	**48.9**	**20.8**
SVD	**1**	✓	-44.4	78.0	-	-57.6	40.7	-
	2	✓	-44.9	115.4	-	-68.7	70.1	-
	3	✓	-62.8	138.8	-	-84.7	88.7	-
	Mean		**-53.3**	**106.9**	**33.3**	**-71.1**	**55.8**	**23.7**
SVE	**1**	✓	-6.2	57.6	-	-48.2	62.5	-
	2	✓	-16.7	73.7	-	-65.3	100.6	-
	3	✓	-10.3	52.9	-	-49.4	54.3	-
	Mean		**-11.2**	**61.3**	**18.2**	**-55.7**	**68.2**	**24.9**
ESB	**8**		-43.7	44.3	-	-46.1	126.3	-
	9		-67.6	360.1	-	-87.1	169.2	-
	Mean		**-57.4**	**29.4**	**80.2**	**-67.0**	**129.0**	**109.9**
SVC/D/E Mean			-	-	-	-64.9	59.2	9.8
SVA/C/D/E (Preferred) Mean "HEBh"			**-**	-	-	**-60.6**	**83.9**	**15.3**
All Areas Mean			-	-	-	-62.4	89.0	14.1
M Component Mean "HEBm"			**40.9**	**34.9**	***dp*=5.9 *dm*=4.1**	**-**	**-**	**-**

Table S3. Previous paleopoles reported from the Pilbara Craton. Subscript "geo" indicates geographic (*in situ*) coordinates; "tc" indicates tilt-corrected (stratigraphic) coordinates. For poles not calculated from site-mean VGPs, α_{95} is reported as the semiminor and semimajor axes (dp, dm) of the pole error ellipse in degrees. α_{95} in degrees; λ in degrees N; Φ in degrees E. For pole DFM, the two rows in geographic coordinates are for each limb of the fold test (DFM1, DFM2). The MB-1 pole is shown, but likely misoriented due to drillcore rotation.

ID	Age (Ma)	λ_{geo}	Φ_{geo}	$\alpha_{95,\,geo}$	λ_{tc}	Φ_{tc}	$\alpha_{95,\,tc}$	Ref
DFM	3464-3471	-17.5	38.4	*dp*=6.8 *dm*=12.5	43.9	86.3	7.2	(*46*)
		73.5	49.1	*dp*=8.3 *dm*=15.2				
DFH	?	18.7	182.9	14.5				(*46*)
DFL	<3465	55.4	132.2	12.5				(*46*)
MB-1	3458-3471	58.5	145.9	6.3	67.4	358.2	6.3	(*83*)
CDm	3350-3515	60.0	154.4	*dp*=5.3 *dm*=10.5	-2.3	186.4	*dp*=7.4 *dm*=12.4	(*49*)
EBm	3335-3350	49.6	17.7	*dp*=3.8 *dm*=6.3	46.5	68.3	*dp*=2.8 *dm*=5.4	(*49*)
RB	~2772				-52.4	178.0	*dp*=6.4 *dm*=9.1	(*81*)
P0	>2772±2				-1.0	93.0	8.0	(*37*)
BRS	2772±2				-4.0	130.0	15.0	(*50*)
P1	~2770				-41.0	160.0	4.0	(*37*)
P2	2766±2				-47.0	153.0	15.0	(*37*)
MJV	>2750±5				-41.0	129.0	20.0	(*37*)
P4-7	~2730				-50.0	138.0	13.0	(*37*)
P8-10	~2715				-59.0	186.0	6.0	(*37*)
SVH	2717±2				-65.0	204.0	12.0	(*37*)
MT7-10	1700-2715				-53.2	203.9	5.3	(*37*)
TPA	~1700?				-37.4	220.3	*dp*=5.7 *dm*=11.3	(*82*)
HP2	~1700?				-35.3	211.9	3.0	(*34*)
HP1	~1500?				-33.9	70.7	8.4	(*34*)
MDS	755±3				43.8	134.1	5.1	(*101*)

Data file S1. Component fits for all samples. Sheets in this excel file contain lists of AF, L, M, H (unforced), and HF (forced) components. Each fit direction is reported in *in-situ* (D_g, I_g) and stratigraphically-corrected (D_s, I_s) coordinates.

Data file S2. Full demagnetization data for all samples. Files with names "[locality].sam" list samples for each locality in the common CIT format. Files with names "[locality].lsq" contain least-squares fits to sample directions. Files with sample names only (extensionless) are NRM demagnetization sequences. These data are readable with the free software "Paleomag X", available from http://cires1.colorado.edu/people/jones.craig/PMag3.html.

REFERENCES AND NOTES

1. W. Bleeker, The late Archean record: A puzzle in ca. 35 pieces. *Lithos* **71**, 99–134 (2003).

2. P. Thurston, Greenstone belts and granite−greenstone terranes: Constraints on the nature of the archean world. *Geosci. Can.*, **42** 10.12789/geocanj.2015.42.081 (2015).

3. M. Tang, K. Chen, R. L. Rudnick, Archean upper crust transition from mafic to felsic marks the onset of plate tectonics. *Science* **351**, 372–375 (2016).

4. N. D. Greber, N. Dauphas, A. Bekker, M. P. Ptáček, I. N. Bindeman, A. Hofmann, Titanium isotopic evidence for felsic crust and plate tectonics 3.5 billion years ago. *Science* **357**, 1271–1274 (2017).

5. M. J. Van Kranendonk, Two types of archean continental crust: Plume and plate tectonics on early earth. *Am. J. Sci.* **310**, 1187–1209 (2010).

6. R. Fischer, T. Gerya, Early earth plume-lid tectonics: A high-resolution 3D numerical modelling approach. *J. Geodyn.* **100**, 198–214 (2016).

7. E. Sizova, T. Gerya, K. Stüwe, M. Brown, Generation of felsic crust in the Archean: A geodynamic modeling perspective. *Precambrian Res.* **271**, 198–224 (2015).

8. D. Chardon, P. Choukroune, M. Jayananda, Strain patterns, décollement and incipient sagducted greenstone terrains in the Archaean Dharwar craton (south India). *J. Struct. Geol.* **18**, 991–1004 (1996).

9. D. Wiemer, C. E. Schrank, D. T. Murphy, L. Wenham, C. M. Allen, Earth's oldest stable crust in the Pilbara Craton formed by cyclic gravitational overturns. *Nat. Geosci.* **11**, 357–361 (2018).

10. A. Lenardic, The diversity of tectonic modes and thoughts about transitions between them. *Philos. Trans. A Math. Phys. Eng. Sci.* **376**, 20170416 (2018).

11. J. H. Bédard, Stagnant lids and mantle overturns: Implications for Archaean tectonics, magmagenesis, crustal growth, mantle evolution, and the start of plate tectonics. *Geosci. Front.* **9**, 19–49 (2018).

12. J. Korenaga, Archean geodynamics and the thermal evolution of Earth. *Geophys. Monogr. Am. Geophys. Union* **164**, 7–32 (2006).

13. B. Keller, B. Schoene, Plate tectonics and continental basaltic geochemistry throughout Earth history. *Earth Planet. Sci. Lett.* **481**, 290–304 (2018).

14. B. Dhuime, C. J. Hawkesworth, P. A. Cawood, C. D. Storey, A change in the geodynamics of continental growth 3 billion years ago. *Science* **335**, 1334–1336 (2012).

15. J. Korenaga, Crustal evolution and mantle dynamics through Earth history. *Philos. Trans. A Math. Phys. Eng. Sci.* **376**, 20170408 (2018).

16. S. B. Shirey, S. H. Richardson, Start of the Wilson cycle at 3 Ga shown by diamonds from subcontinental mantle. *Science* **333**, 434–436 (2011).

17. R. J. Stern, Evidence from ophiolites, blueschists, and ultrahigh-pressure metamorphic terranes that the modern episode of subduction tectonics began in Neoproterozoic time. *Geology* **33**, 557–560 (2005).

18. M. J. Van Kranendonk, R. Hugh Smithies, A. H. Hickman, M. T. D. Wingate, S. Bodorkos, Evidence for mesoarchean (~3.2Ga) rifting of the pilbara craton: The missing link in an early precambrian wilson cycle. *Precambrian Res.* **177**, 145–161 (2010).

19. S. Turner, T. Rushmer, M. Reagan, J.-F. Moyen, Heading down early on? Start of subduction on Earth. *Geology* **42**, 139–142 (2014).

20. D. A. Evans, S. A. Pisarevsky, Plate tectonics on early Earth? Weighing the paleomagnetic evidence, in *When Did Plate Tectonics Begin on Planet Earth*, K. C. Condie, V. Pease, Eds. (Geological Society of America, 2008), vol. **440**, pp. 249–263.

21. P. A. Cawood, A. Kroner, S. Pisarevsky, Precambrian plate tectonics: Criteria and evidence. *GSA Today* **16**, 4–10 (2006).

22. P. A. Cawood, C. J. Hawkesworth, S. A. Pisarevsky, B. Dhuime, F. A. Capitanio, O. Nebel, Geological archive of the onset of plate tectonics. *Philos. T. R. Soc. A* **376**, 20170405 (2018).

23. C. O'Neill, S. Turner, T. Rushmer, The inception of plate tectonics: A record of failure. *Phil. Trans. R. Soc. A*. **376**, 20170414 (2018).

24. K. J. Matthews, K. T. Maloney, S. Zahirovic, S. E. Williams, M. Seton, R. D. Müller, Global plate boundary evolution and kinematics since the late Paleozoic. *Global Planet. Change* **146**, 226–250 (2016).

25. J. J. Fuentes, J. W. Crowley, R. Dasgupta, J. X. Mitrovica, The influence of plate tectonic style on melt production and CO_2 outgassing flux at mid-ocean ridges. *Earth Planet. Sci. Lett.* **511**, 154–163 (2019).

26. A. Hickman, Pilbara Supergroup of the East Pilbara Terrane, Pilbara Craton: Updated lithostratigraphy and comments on the influence of vertical tectonics. *GSWA Annual Review* **10**, 50–59 (2009).

27. M. J. Van Kranendonk, H. R. Smithies, A. H. Hickman, D. C. Champion, Review: Secular tectonic evolution of Archean continental crust: Interplay between horizontal and vertical processes in the formation of the Pilbara Craton, Australia, *Terra Nova* **19**, 1–38 (2007).

28. M. J. Van Kranendonk, Geological Survey of Western Australia, *Revised Lithostratigraphy of Archean Supracrustal and Intrusive Rocks in the Northern Pilbara Craton, Western Australia* (Geological Survey of Western Australia, 2006).

29. M. J. Van Kranendonk, *Structural Geology of the Central Part of the Lalla Rookh Western Shaw Structural Corridor, Pilbara Craton, Western Australia* (Geological Survey of Western Australia, 2008).

30. M. J. Van Kranendonk, W. J. Collins, Timing and tectonic significance of Late Archaean, sinistral strike-slip deformation in the Central Pilbara Structural Corridor, Pilbara Craton, Western Australia. *Precambrian Research* **88**, 207–232 (1998).

31. M. J. Van Kranendonk, *Geology of the North Shaw 1: 100 000 Sheets: Sheets 2755* (Geological Survey of Western Australia, 2000).

32. B. Rasmussen, I. R. Fletcher, S. Sheppard, Isotopic dating of the migration of a low-grade metamorphic front during orogenesis. *Geology* **33**, 773–776 (2005).

33. P. A. Cawood, I. M. Tyler, Assembling and reactivating the Proterozoic Capricorn Orogen: Lithotectonic elements, orogenies, and significance. *Precambrian Res.* **128**, 201–218 (2004).

34. Z. X. Li, W. Guo, C. M. C. A. Powell, Timing and genesis of Hamersley BIF-hosted iron deposits: A new palaeomagnetic interpretation. MERIWA Project M242, (Minerals & Energy Research Institute of Western Australia, 2000), vol. 199.

35. G. Pullaiah, E. Irving, K. L. Buchan, D. J. Dunlop, Magnetization changes caused by burial and uplift. *Earth Planet. Sci. Lett.* **28**, 133–143 (1975).

36. L. Tauxe, G. S. Watson, The fold test: An eigen analysis approach. *Earth Planet. Sci. Lett.* **122**, 331–341 (1994).

37. G. Strik, T. S. Blake, T. E. Zegers, S. H. White, C. G. Langereis, Palaeomagnetism of flood basalts in the Pilbara Craton, Western Australia: Late Archaean continental drift and the oldest known reversal of the geomagnetic field, *J. Geophys. Res. Solid Earth* **108**, 2551 (2003).

38. D. Glenn, D. LeSage, R. Fu, B. Weiss, R. Walsworth, *APS Division of Atomic, Molecular and Optical Physics Meeting Abstracts* (2015), vol. 1, 1088 pp.

39. R. Huang, C.-T. Lin, W. Sun, X. Ding, W. Zhan, J. Zhu, The production of iron oxide during peridotite serpentinization: Influence of pyroxene. *Geosci. Front.* **8**, 1311–1321 (2017).

40. R. Day, M. Fuller, V. A. Schmidt, Hysteresis properties of titanomagnetites: Grain-size and compositional dependence. *Phys. Earth Planet. In.* **13**, 260–267 (1977).

41. D. J. Dunlop, Theory and application of the Day plot (M_{rs}/M_s versus H_{cr}/H_c) 1. Theoretical curves and tests using titanomagnetite data. *J. Geophys. Res. Solid Earth* **107**, EPM 4-1–EPM 4-22 (2002).

42. D. Wang, R. Van der Voo, D. R. Peacor, Low-temperature alteration and magnetic changes of variably altered pillow basalts. *Geophys. J. Int.* **164**, 25–35 (2006).

43. E. J. W. Verwey, Electronic conduction of magnetite (Fe_3O_4) and its transition point at low temperatures. *Nature* **144**, 327–328 (1939).

44. A. V. Smirnov, J. A. Tarduno, D. A. D. Evans, Evolving core conditions ca. 2 billion years ago detected by paleosecular variation. *Phys. Earth Planet. In.* **187**, 225–231 (2011).

45. M. W. McElhinny, P. L. McFadden, Palaeosecular variation over the past 5 Myr based on a new generalized database. *Geophys. J. Int.* **131**, 240–252 (1997).

46. M. W. McElhinny, W. E. Senanayake, Paleomagnetic evidence for the existence of the geomagnetic field 3.5 Ga ago. *J. Geophys. Res. Solid Earth* **85**, 3523–3528 (1980).

47. P. V. Doubrovine, T. Veikkolainen, L. J. Pesonen, E. Piispa, S. Ots, A. V. Smirnov, E. V. Kulakov, A. J. Biggin, Latitude dependence of geomagnetic paleosecular variation and its relation to the frequency of magnetic reversals: Observations from the cretaceous and jurassic. *Geochem. Geophys. Geosyst.* **20**, 1240–1279 (2019).

48. A. H. Saad, Paleomagnetism of Franciscan ultramafic rocks from Red Mountain, California, *J. Geophys. Res.* **74**, 6567–6578 (1969).

49. K. Bradley, B. P. Weiss, R. Buick, Records of geomagnetism, climate, and tectonics across a Paleoarchean erosion surface. *Earth Planet. Sci. Lett.* **419**, 1–13 (2015).

50. D. Evans, A. V. Smirnov, A. Gumsley, Paleomagnetism and U–Pb geochronology of the black range dykes, Pilbara Craton, Western Australia: A neoarchean crossing of the polar circle *Aust. J. Earth Sci.* **64**, 225–237 (2017).

51. T. H. Torsvik, R. van der Voo, U. Preeden, C. Mac Niocaill, B. Steinberger, P. V. Doubrovine, D. J. J. van Hinsbergen, M. Domeier, C. Gaina, E. Tohver, J. G. Meert, P. J. A. McCausland, L. R. M. Cocks, Phanerozoic polar wander, palaeogeography and dynamics. *Earth-Sci. Rev.* **114**, 325–368 (2012).

52. C. O'Neill, A. Lenardic, L. Moresi, T. H. Torsvik, C.-T. A. Lee, Episodic Precambrian subduction. *Earth Planet. Sci. Lett.* **262**, 552–562 (2007).

53. V. C. Tsai, D. J. Stevenson, Theoretical constraints on true polar wander. *J. Geophys. Res. Solid Earth* **112**, B05415 (2007).

54. J. Creveling, J. Mitrovica, N.-H. Chan, K. Latychev, I. Matsuyama, Mechanisms for oscillatory true polar wander. *Nature* **491**, 244–248 (2012).

55. J. L. Kirschvink, The least-squares line and plane and the analysis of palaeomagnetic data. *Geophys. J. Roy. Astron. Soc.* **62**, 699–718 (1980).

56. D. R. Glenn, R. R. Fu, P. Kehayias, D. le Sage, E. A. Lima, B. P. Weiss, R. L. Walsworth, Micrometer-scale magnetic imaging of geological samples using a quantum diamond microscope. *Geochem. Geophys. Geosyst.* **18**, 3254–3267 (2017).

57. E. A. Lima, B. P. Weiss, Obtaining vector magnetic field maps from single-component measurements of geological samples. *J. Geophys. Res. Solid Earth* **114**, B06102 (2009).

58. R. R. Doell, Paleomagnetic secular variation study of lavas from the Massif central, France, *Earth Planet. Sci. Lett.* **8**, 352–362 (1970).

59. A. Cox, Latitude dependence of the angular dispersion of the geomagnetic field. *Geophys. J. Int.* **20**, 253–269 (1970).

60. N. D. Watkins, Brunhes epoch geomagnetic secular variation on Reunion Island. *J. Geophys. Res.* **78**, 7763–7768 (1973).

61. B. Efron, *The Jackknife, the Bootstrap, and Other Resampling Plans* (Siam, 1982), vol. 38.

62. C. Hawkesworth, P. Cawood, T. Kemp, C. Storey, B. Dhuime, Geochemistry. A matter of preservation. *Science* **323**, 49–50 (2009).

63. M. Pujol, B. Marty, R. Burgess, G. Turner, P. Philippot, Argon isotopic composition of Archaean atmosphere probes early Earth geodynamics. *Nature* **498**, 87–90 (2013).

64. L. D. Ashwal, G. M. Bybee, Crustal evolution and the temporality of anorthosites. *Earth-Sci. Rev.* **173**, 307–330 (2017).

65. M. E. Barley, B. Krapez, D. I. Groves, R. Kerrich, The Late Archaean bonanza: Metallogenic and environmental consequences of the interaction between mantle plumes, lithospheric tectonics and global cyclicity. *Precambrian Res.* **91**, 65–90 (1998).

66. S. Tappe, K. A. Smart, D. G. Pearson, A. Steenfelt, A. Simonetti, Craton formation in Late Archean subduction zones revealed by first Greenland eclogites. *Geology* **39**, 1103–1106 (2011).

67. D. Pearson, N. Wittig, The formation and evolution of cratonic mantle lithosphere–evidence from mantle xenoliths. *Treatise on Geochemistry* **2014**, 255–292 (2014).

68. N. S. C. Simon, R. W. Carlson, D. G. Pearson, G. R. Davies, The origin and evolution of the Kaapvaal cratonic lithospheric mantle. *J. Petrol.* **48**, 589–625 (2007).

69. R. H. Smithies, M. J. Van Kranendonk, D. C. Champion, The Mesoarchean emergence of modern-style subduction. *Gondw. Res.* **11**, 50–68 (2007).

70. R. H. Smithies, D. C. Champion, K. F. Cassidy, Formation of Earth's early Archaean continental crust. *Precambrian Res.* **127**, 89–101 (2003).

71. A. M. Bauer, C. M. Fisher, J. D. Vervoort, S. A. Bowring, Coupled zircon Lu–Hf and U–Pb isotopic analyses of the oldest terrestrial crust, the >4.03 Ga Acasta Gneiss Complex. *Earth Planet. Sci. Lett.* **458**, 37–48 (2017).

72. E. A. Bell, T. M. Harrison, M. T. McCulloch, E. D. Young, Early Archean crustal evolution of the Jack Hills Zircon source terrane inferred from Lu–Hf, $^{207}Pb/^{206}Pb$, and $\delta^{18}O$ systematics of Jack Hills zircons. *Geochim. Cosmochim. Acta* **75**, 4816–4829 (2011).

73. T. E. Zegers, D. R. Nelson, J. R. Wijbrans, S. H. White, SHRIMP U-Pb zircon dating of Archean core complex formation and pancratonic strike-slip deformation in the East Pilbara Granite-Greenstone Terrain. *Tectonics* **20**, 883–908 (2001).

74. A. Kloppenburg, S. H. White, T. E. Zegers, Structural evolution of the warrawoona greenstone belt and adjoining granitoid complexes, Pilbara Craton, Australia: Implications for archaean tectonic processes. *Precambrian Res.* **112**, 107–147 (2001).

75. M. Bickle, L. F. Bettenay, H. J. Chapman, D. I. Groves, N. J. McNaughton, I. H. Campbell, J. R. de Laeterd, Origin of the 3500-3300 Ma calc-alkaline rocks in the Pilbara Archaean: Isotopic and geochemical constraints from the Shaw Batholith. *Precambrian Res.* **60**, 117–149 (1993).

76. H. Furnes, M. de Wit, H. Staudigel, M. Rosing, K. Muehlenbachs, A vestige of Earth's oldest ophiolite. *Science* **315**, 1704–1707 (2007).

77. F. E. Jenner, V. C. Bennett, G. Yaxley, C. R. L. Friend, O. Nebel, Eoarchean within-plate basalts from southwest Greenland. *Geology* **41**, 327–330 (2013).

78. C. M. Fisher, J. D. Vervoort, Using the magmatic record to constrain the growth of continental crust—The Eoarchean zircon Hf record of Greenland. *Earth Planet. Sci. Lett.* **488**, 79–91 (2018).

79. P. Boehnke, E. A. Bell, T. Stephan, R. Trappitsch, C. B. Keller, O. S. Pardo, A. M. Davis, T. M. Harrison, M. J. Pellin, Potassic, high-silica Hadean crust. *Proc. Natl. Acad. Sci. U.S.A.* **115**, 6353–6356 (2018).

80. O. Laurent, H. Martin, J. F. Moyen, R. Doucelance, The diversity and evolution of late-Archean granitoids: Evidence for the onset of "modern-style" plate tectonics between 3.0 and 2.5 Ga. *Lithos* **205**, 208–235 (2014).

81. P. W. Schmidt, B. J. J. Embleton, Prefolding and overprint magnetic signatures in Precambrian (~ 2.9–2.7 Ga) igneous rocks from the Pilbara Craton and Hamersley Basin, NW Australia. *J. Geophys. Res. Solid Earth* **90**, 2967–2984 (1985).

82. P. W. Schmidt, D. A. Clark, Palaeomagnetism and magnetic anisotropy of Proterozoic banded-iron formations and iron ores of the Hamersley Basin, Western Australia, *Precambrian Res.* **69**, 133–155 (1994).

83. Y. Suganuma, Y. Hamano, S. Niitsuma, M. Hoashi, T. Hisamitso, N. Niitsuma, K. Kodama, M. Nedachi, Paleomagnetism of the Marble Bar Chert Member, Western Australia: Implications for apparent polar wander path for Pilbara craton during Archean time. *Earth Planet. Sci. Lett.* **252**, 360–371 (2006).

84. M. T. D. Wingate, in *A Palaeomagnetic Test of the Kaapvaal - Pilbara (Vaalbara) Connection at 2.78 Ga*. (1998), vol. 101, pp. 257–274.

85. S. Denyszyn, J. Feinberg, P. R. Renne, G. R. Scott, in *Revisiting the Age and Paleomagnetism of the Modipe Gabbro of South Africa*. (2013), vol. 238, pp. 176–185.

86. M. O. de Kock, D. A. D. Evans, N. J. Beukes, Validating the existence of Vaalbara in the Neoarchean. *Precambrian Res.* **174**, 145–154 (2009).

87. G. Strik, M. J. De Wit, C. G. Langereis, Palaeomagnetism of the neoarchaean pongola and ventersdorp supergroups and an appraisal of the 3.0–1.9 Ga apparent polar wander path of the Kaapvaal Craton, Southern Africa. *Precambrian Res.* **153**, 96–115 (2007).

88. A. J. Biggin, M. J. de Wit, C. G. Langereis, T. E. Zegers, S. Voûte, M. J. Dekkers, K. Drost, Palaeomagnetism of Archaean rocks of the Onverwacht Group, Barberton Greenstone Belt (southern Africa): Evidence for a stable and potentially reversing geomagnetic field at ca. 3.5 Ga. *Earth Planet. Sci. Lett.* **302**, 314–328 (2011).

89. Y. Usui, J. A. Tarduno, M. Watkeys, A. Hofmann, R. D. Cottrell, Evidence for a 3.45-billion-year-old magnetic remanence: Hints of an ancient geodynamo from conglomerates of South Africa. *Geochem. Geophys. Geosyst.* **10**, Q09Z07 (2009).

90. A. Yoshihara, Y. Hamano, Paleomagnetic constraints on the Archean geomagnetic field intensity obtained from komatiites of the Barberton and Belingwe greenstone belts, South Africa and Zimbabwe. *Precambrian Res.* **131**, 111–142 (2004).

91. T. E. Zegers, M. J. de Wit, J. Dann, S. H. White, Vaalbara, Earth's oldest assembled continent? A combined structural, geochronological, and palaeomagnetic test. *Terra Nova* **10**, 250–259 (1998).

92. E. Cheney, in *Extended Abstracts Geocongress*. (1990), vol. 90, pp. 88–91.

93. P. W. Schmidt, A review of precambrian palaeomagnetism of Australia: Palaeogeography, supercontinents, glaciations and true polar wander. *Gondw. Res.* **25**, 1164–1185 (2014).

94. A. H. Hickman, *Northwest Pilbara Craton: A Record of 450 Million Years in the Growth of Archean Continental Crust* (Report 160, Geological Survey of Western Australia, East Perth, Western Australia, 2016), 104 pp.

95. P. W. Layer, A. Kröner, M. McWilliams, An archean geomagnetic reversal in the Kaap Valley Pluton, South Africa, *Science* **273**, 943–946 (1996).

96. P. W. Layer, M. Lopez-Martinez, A. Kröner, D. York, M. McWilliams, Thermochronometry and palaeomagnetism of the Archaean Nelshoogte Pluton, South Africa, *Geophys. J. Int.* **135**, 129–145 (1998).

97. J. A. Tarduno, R. D. Cottrell, M. K. Watkeys, D. Bauch, Geomagnetic field strength 3.2 billion years ago recorded by single silicate crystals. *Nature* **446**, 657–660 (2007).

98. S. Letts, T. H. Torsvik, S. J. Webb, L. D. Ashwal, Palaeomagnetism of the 2054 Ma Bushveld Complex (South Africa): Implications for emplacement and cooling. *Geophys. J. Int.* **179**, 850–872 (2009).

99. J. R. Lowrey, D. A. Wyman, T. J. Ivanic, M. P. Roberts, Platy Pyroxene: New insights into spinifex texture. *J. Petrol.* **58**, 1671–1700 (2017).

100. S. Bouquain, N. T. Arndt, E. Hellebrand, F. Faure, Crystallochemistry and origin of pyroxenes in komatiites. *Contrib. Mineral. Petrol.* **158**, 599 (2009).

101. M. T. Wingate, J. W. Giddings, Age and palaeomagnetism of the Mundine Well dyke swarm, Western Australia: Implications for an Australia–Laurentia connection at 755 Ma. *Precambrian Res.* **100**, 335–357 (2000).